Quantifying dyke-induced graben and dyke structure using 3D seismic reflection data

Craig Magee[1]*, Victoria Love[1], Karima Fayez[1], Billy J. Andrews[2], Sam Rivas-Dorado[3], Christopher A-L Jackson[4], Claire Orlov[1], Emma Bramham[1]

[1] School of Earth and Environment, University of Leeds, Leeds, UK

[2] School of Geography, Earth and Environmental Sciences, University of Plymouth, Plymouth, Devon, PL4 8AA, UK

[3] Deparatamento de Geodinámica, Estratigrafía y Paleontología, Universidad Complutense de Madrid, Madrid, 28040, Spain

[4] Basins Research Group (BRG), Department of Earth Science and Engineering, Imperial College London, SW7 2BP, England, UK

**Corresponding author (e-mail: c.magee@leeds.ac.uk)*

Abstract

During dyke intrusion, tensile stresses concentrated within the overlying rock may lead to the formation of normal faults. These faults typically form graben-bounding pairs that are sub-parallel to, and dip toward, the upper tip of their underlying dyke. Many studies use geometric properties extracted from the surface expression of such dyke-induced faults to estimate the geometry of subsurface dykes. These methods assume dyke-induced faults are planar and nucleate at the surface. However, recent investigations of the 3D structure of dyke-induced faults using seismic reflection data confirm they can be non-planar and have complex growth histories. Here, we use 3D seismic reflection surveys from offshore NW Australia to: (1) examine how the surface expression of dyke-induced faults relates to subsurface dyke geometry and depth; and (2) test whether subjective bias may influence the quantitative analyses of dyke-induced faults. We show displacement and dip vary across dyke-induced faults, supporting previous suggestions that faults nucleate between dyke upper tips and the free surface. We also find that depths of dyke upper tips predicted using graben width and area of loss measurements, whilst sensitive to fault dip variations and interpretation biases, are often similar to measured dyke depths. Both measured and

predicted dyke depths vary by several hundred metres along-strike, which we relate to the preservation of dyke heads, segmentation, and/or magma density changes. Overall, we show reflection seismology provides a better understanding of the 3D structure of dyke-induced faults and their relationship to the geometry and emplacement dynamics of their causal dykes.

1. Introduction

Igneous dykes facilitate magma transport and their intrusion generates both extensional and compressional stresses (Fig. 1A) (e.g., Rivalta et al., 2015, Rubin, 1993). Within the upper crust, dyke intrusion and opening is expected to concentrate tensile stresses above the dyke upper tip and in two elongate, sub-parallel zones at the free surface (Fig. 1A) (e.g., Koehn et al., 2019, Pollard et al., 1983, Rubin, 1992, Rubin & Pollard, 1988). Shear failure within this extensional stress field produces graben-bounding normal faults that strike sub-parallel to the underlying dyke and which extend from the dyke's upper tip to zones of maximum tensile stress at the surface (Fig. 1A) (e.g., Pollard et al., 1983, Trippanera et al., 2015a). In many active and ancient volcanic systems, on Earth and other planetary bodies, we can examine the surface expression of such dyke-induced faults and quantify their geometry, displacement, and kinematics (e.g., Perrin et al., 2022, Pollard et al., 1983, Rivas-Dorado et al., 2021, Trippanera et al., 2015a, Wilson & Head, 2002, Xu et al., 2016). We expect these fault properties to relate to the underlying dyke location, size, shape, and intrusion dynamics (e.g., Dumont et al., 2017, Rivas-Dorado et al., 2021, Trippanera et al., 2015a). Studying dyke-induced faults thus allows us to infer the structure and dynamics of subsurface dykes, which is crucial to understanding volcanic activity and the role of dyking in crustal extension (e.g., Dumont et al., 2016, Rivas-Dorado et al., 2021, Trippanera et al., 2015b, Wilson & Head, 2002, Xu et al., 2016).

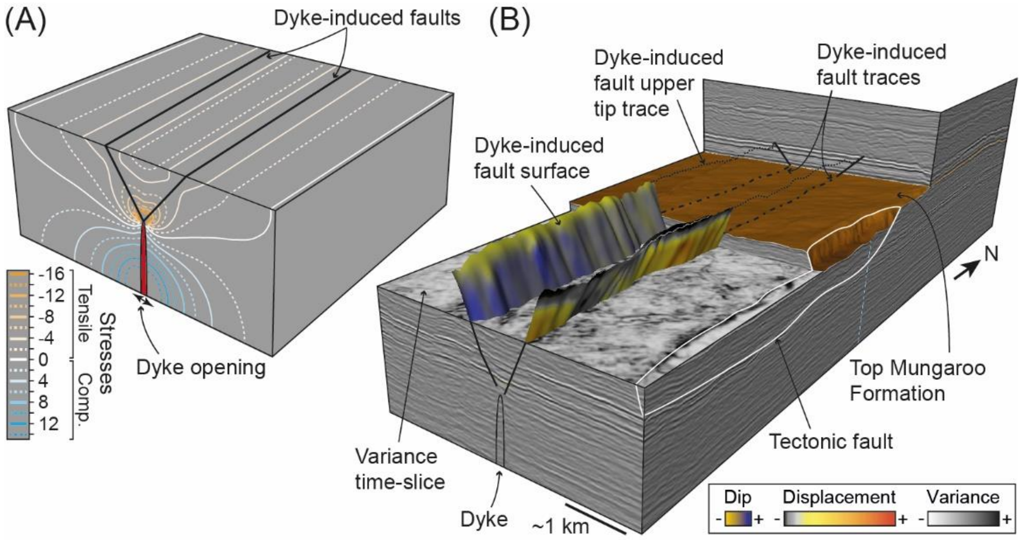

Figure 1: (A) Schematic 3D block diagram showing the modelled stress distribution around an opening dyke, and the location of expected dyke-induced faults (based on Rubin, 1992). (B) 3D seismic reflection data from the Chandon 3D seismic survey, offshore NW Australia, detailing the seismic expression of dykes and dyke-induced faults (based on Magee & Jackson, 2020b). Fault dip and displacement variations are shown on the opposing faults.

Several previous studies have used the width of dyke-induced graben and fault heaves to estimate the depth to dyke upper tips and dyke thickness, respectively (e.g., Hjartardóttir et al., 2016, Perrin et al., 2022, Rivas-Dorado et al., 2021, Rubin, 1992, Rubin & Pollard, 1988, Trippanera et al., 2015b). These predictions assume that dyke-induced faults are planar and project down-dip to intersect at the dyke upper tip (Fig. 1A), and that their cumulative heaves are equivalent to dyke thickness (e.g., Magee & Jackson, 2020b). Physical, numerical, and analytical models support these assumptions (e.g., Hardy, 2016, Koehn et al., 2019, Mastin & Pollard, 1988, Pollard et al., 1983, Trippanera et al., 2015b), but it is difficult to test their validity because: (1) we lack field exposures that reveal the 3D structure of dyke *and* dyke-induced fault systems; and (2) models of ground movement related to active dyke-induced faulting are typically non-unique (e.g., Wright et al., 2006).

Reflection seismology allows us to image entire dyke and dyke-induced fault systems in 3D at a decametre-scale (Fig. 1B) (Bosworth et al., 2015, Magee & Jackson, 2020a, Magee & Jackson, 2020b). For example, using seismic reflection data from offshore NW Australia, Magee and Jackson (2020b) show that fault displacement, heave, and dip varied laterally and vertically across two buried dyke-induced faults (Fig. 1B). Heterogeneity in fault dip indicates dyke-induced faults are not always planar, as is commonly assumed, and that their surficial heave may not fully reflect the extension the faults accommodate (Fig. 1B) (Magee & Jackson, 2020b). These findings question the accuracy of dyke locations, sizes, and shapes estimated from the surface expression of dyke-induced faults (Magee & Jackson, 2020b). However, extracting quantitative data (e.g., dyke-induced fault properties) from seismic reflection data is subject to several objective and subjective sources of uncertainty (e.g., Alcalde et al., 2017a, Bond et al., 2007, Dimmen et al., 2022, Faleide et al., 2021, Wilson et al., 2019). We thus need to explore how these sources of uncertainty may affect interpretation of dyke-induced fault data extracted from seismic reflection volumes.

Here, we use two 3D seismic reflection datasets from offshore NW Australia to extend the study of Magee and Jackson (2020b). We specifically test: (1) if other dyke-induced fault pairs in the region show similar variations in displacement and dip across their surface (e.g., Fig. 1B) (Magee & Jackson, 2020b); (2) the reliability of trigonometry and area of loss methods for estimating dyke upper tip depths, which we henceforth refer to as top-dyke depths, from dyke-induced graben properties (e.g., Pollard et al., 1983, Rivas-Dorado et al., 2021, Trippanera et al., 2015b); and (3) how sources of uncertainty affect variations in measured or calculated fault, graben, or dyke properties (e.g., Bond et al., 2007, Faleide et al., 2021). To achieve our aims, we compile and calculate fault property data from footwall and hanging wall cut-offs mapped by four individuals from the same faults. We present data for dyke-induced fault pairs above three dykes and show displacement and dip is variable across them all, consistent with the findings of Magee and Jackson (2020b). Although interpretation bias can introduce measurement errors, consistency between datasets produced by different individuals suggests we can, at least to a first order, relate the surface expression of dyke-induced faults to dyke geometry (cf. Magee & Jackson, 2020b). However, building confidence in estimated dyke parameters requires knowledge of how fault properties, particularly dip, change with depth. Unfortunately, this subsurface information is rarely available for active volcanic settings or other planetary bodies, but we suggest empirical data and relationships derived from reflection seismic data could help reduce uncertainty (Magee & Jackson, 2020b).

2. Geological setting

The Northern Carnarvon Basin, located offshore NW Australia, developed during several phases of rifting between Australia and Greater India in the Late Carboniferous-to-Early Cretaceous (Fig. 2) (e.g., Direen et al., 2008, Stagg et al., 2004, Tindale et al., 1998). The Exmouth Plateau is located in the south-west of the Northern Carnarvon Basin, and is a region of <10 km thick continental crust overlain by a <18 km thick sedimentary sequence (Fig. 2C) (e.g., Exon et al., 1992, Karner & Driscoll, 1999, Pryer et al., 2002). Rifting of the Exmouth Plateau began in the Late Triassic-to-Jurassic, forming an array of ~N-S striking, large (often >1 km throw) normal faults within pre-rift, fluvio-deltaic sedimentary rocks of the Mungaroo Formation (Figs 2B and C) (e.g., Bilal & McClay, 2022, Bilal et al., 2018, Stagg et al., 2004). The Exmouth Plateau was sediment-starved during this phase of rifting, thus contains a relatively condensed (≲100 m thick), late Triassic-to-Early Jurassic marine succession (e.g., Figs 2B and C) (e.g., Exon et al., 1992, Karner & Driscoll, 1999). This latest Triassic-to-Early Jurassic strata is separated from the Late Jurassic, marine Dingo Claystone by the end Callovian regional unconformity (Fig. 2B) (e.g., Bilal et al., 2018, Tindale et al., 1998, Yang & Elders, 2016). Tectonic faulting reduced or ceased in the Late Jurassic across the North Carnarvon Basin, but renewed after formation of the Base Cretaceous unconformity (latest Tithonian; ~148 Ma) and during deposition of the Tithonian–Valanginian (~148–138 Ma), marine Barrow Group (Fig. 2B) (e.g., Gartrell et al., 2016, Paumard et al., 2018, Reeve et al., 2016). This renewed faulting produced N-S to NE-SW-striking, low-throw (<0.1 km) normal faults (e.g., Black et al., 2017). Continental break-up eventually occurred along the western and southern margins of the Exmouth Plateau in the Early Cretaceous (Valanginian–Hauterivian; ~135–130 Ma), followed by thermal subsidence and passive margin development (Figs 2B and C) (e.g., Direen et al., 2008, Reeve et al., 2021, Robb et al., 2005).

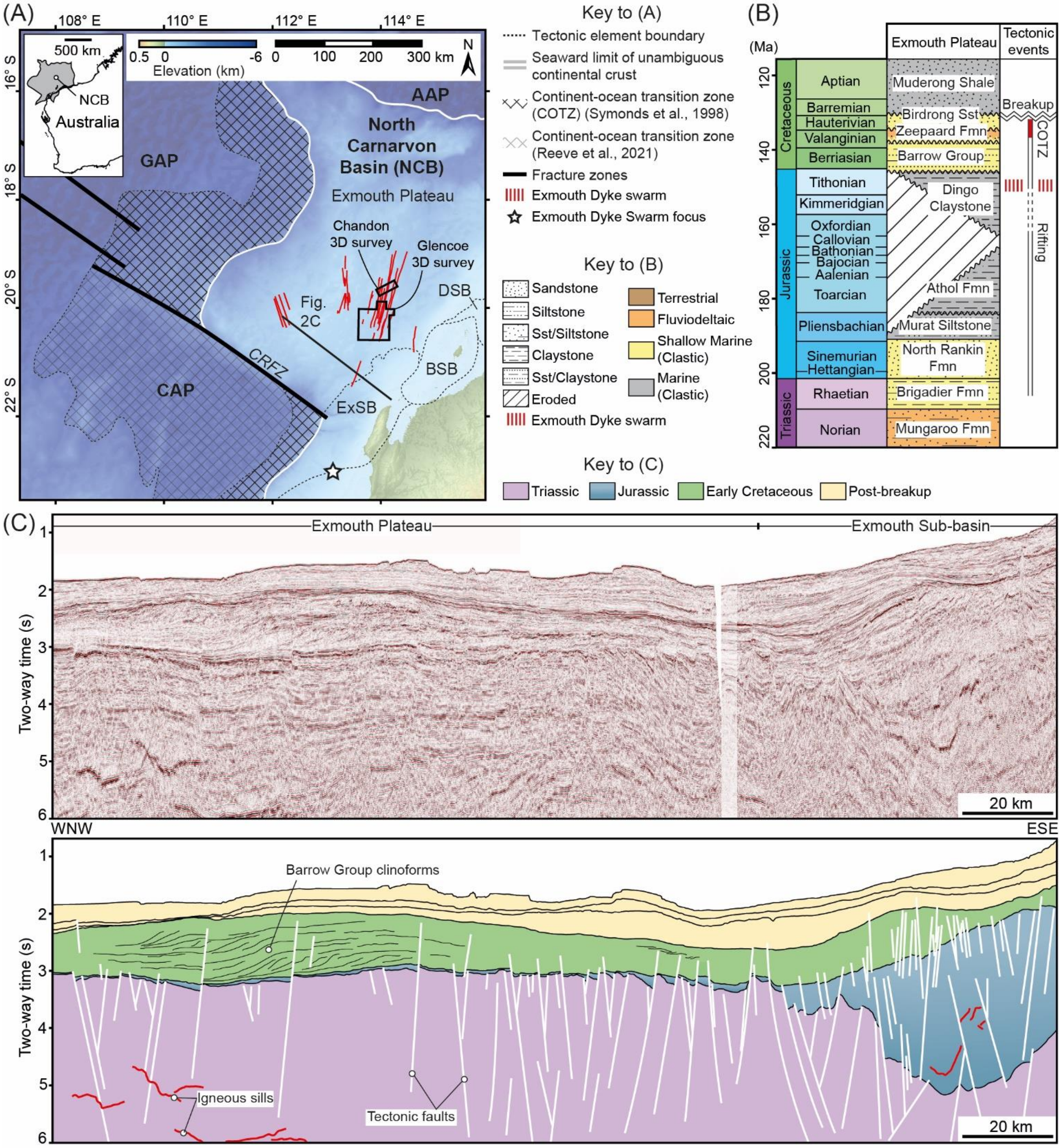

Figure 2: (A) Map of offshore NW Australia highlighting principal tectonic elements: ExSB = Exmouth Sub-basin, BSB = Barrow Sub-basin, DSB = Dampier Sub-basin, CAP = Cuvier Abyssal Plain, GAP = Gascoyne Abyssal Plain, AAP = Argo Abyssal Plain, CRFZ = Cape Range Fracture Zone. Elevation data are based on the 2009 Australian Bathymetry and Topography grid (Geoscience Australia). The Exmouth Dyke Swarm is also shown (Magee & Jackson, 2020a). (B) Tectono-stratigraphic column for the Exmouth Plateau (based on Hocking et al., 1987, Longley et al., 2002, Magee & Jackson, 2020a,

Tindale et al., 1998). (C) Uninterpreted and interpreted 2D seismic line across the Exmouth Plateau and Exmouth Sub-basin showing the upper part of the sedimentary sequence (modified from Norcliffe et al., 2021).

2.1. The Exmouth Dyke Swarm and dyke-induced faults

Seismic reflection data reveal a swarm of sub-vertical, low-amplitude zones that disrupt stratigraphic reflections within (and below) the Mungaroo Formation across the Exmouth Plateau (e.g., Figs 1B, 3A, and C) (Magee & Jackson, 2020a). Borehole data confirm these vertical zones of disruption correspond to dykes, each likely 10's of metres thick, belonging to the Exmouth Dyke Swarm (Magee & Jackson, 2020a). These dykes are 10's–100's km long and appear to radiate outwards from focal area within the Cuvier Margin, from which they likely propagated laterally northwards (e.g., Figs 2A) (Magee & Jackson, 2020a). A series of graben occur directly above and along the dykes, with the oppositely dipping faults intersecting at the dyke upper tips (e.g., Figs 1B and 3); these have been interpreted as dyke-induced faults (Magee & Jackson, 2020a, Magee & Jackson, 2020b). The dyke-induced faults offset siliciclastic Triassic-to-Jurassic strata, and terminate upwards at the Base Cretaceous unconformity, which is inferred to mark a syn-faulting free surface (i.e. the seabed; e.g., Figs 3A and B) (Magee & Jackson, 2020a, Magee & Jackson, 2020b). Within the dyke-induced graben are numerous pit craters, which extend from dyke upper tips or dyke-induced fault planes up into the Upper Jurassic Dingo Claystone (e.g., Fig. 3B) (Magee & Jackson, 2020a, Magee et al., 2022).

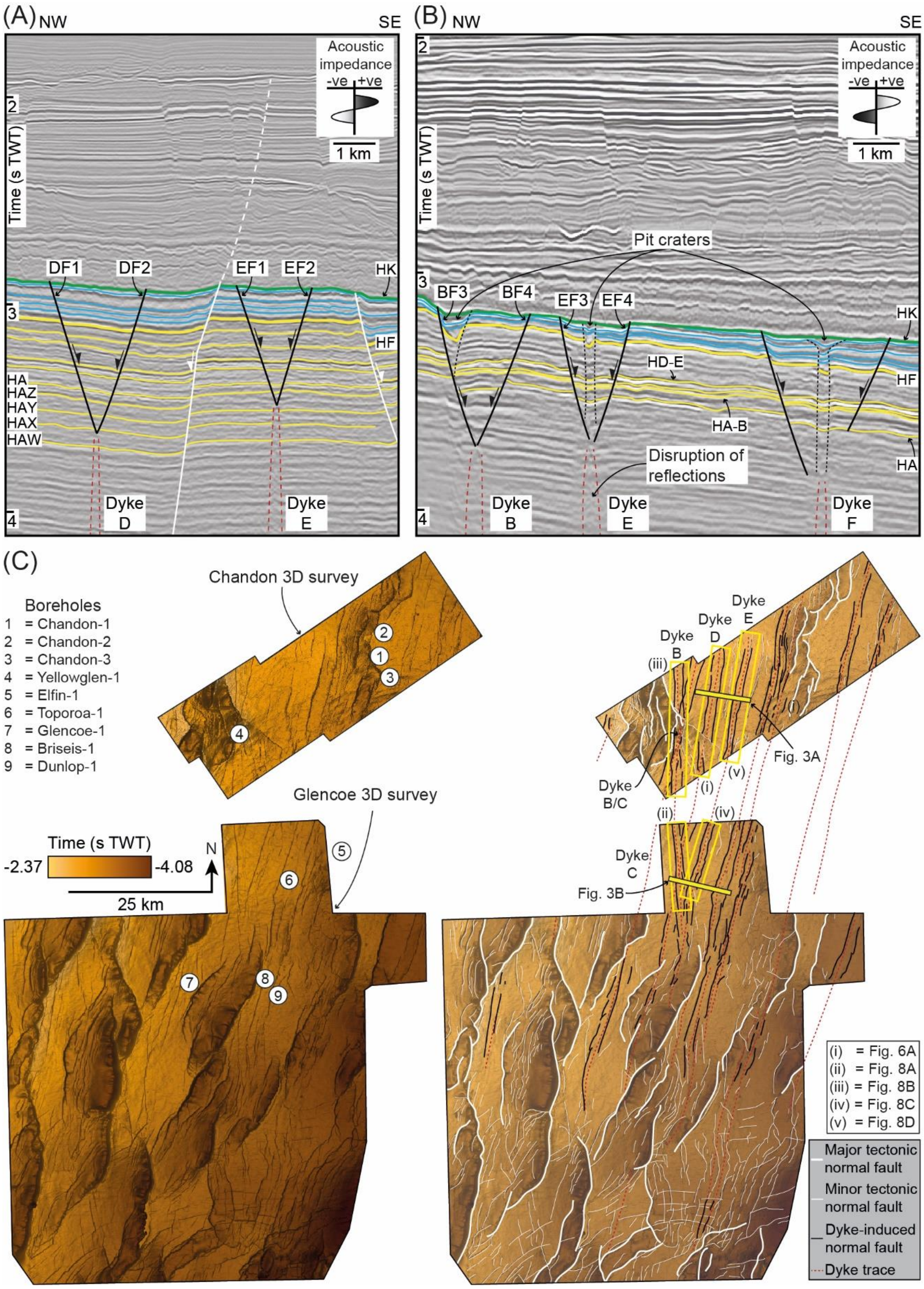

Figure 3: (A and B) Interpreted seismic sections showing dykes, dyke-induced faults, and stratigraphic horizons (HK–HAW) mapped in the Chandon and Glencoe 3D surveys. Yellow horizons are Triassic, blue horizons are Jurassic, and the green horizon marks the Base Cretaceous Unconformity (HK). Some tectonic faults and pit craters are also highlighted (Magee & Jackson, 2020a). Line locations shown in

(C) and insets show how a downwards positive (+ve) or negative (-ve) change in acoustic impedance affects reflection colour. Uninterpreted sections shown in Supplementary Figure S2. (C) Uninterpreted and interpreted time-structure map of the Top Mungaroo Formation (horizon HF) in the Chandon and Glencoe 3D surveys, with tectonic and dyke-induced faults marked. Boreholes used in the study as well as underlying dyke traces are also shown (Magee & Jackson, 2020a).

3. Data and methods

3.1. Data

We use the Chandon and Glencoe 3D seismic reflection surveys to analyse dyke-induced faults above three dykes (dykes B, D, and E; Fig. 3). Both seismic surveys are time-migrated, processed to zero-phase, and have bin size of 25 m; Chandon has a record length of 6 seconds two-way time (s TWT), whereas Glencoe extends down to 8 s TWT. The Chandon 3D survey has a SEG reverse polarity, whereby a positive reflection coefficient (indicating a downward increase in acoustic impedance) corresponds to a trough (black) reflection and a negative reflection coefficient (indicating downward decrease in acoustic impedance) is marked by a peak (white) reflection (Fig. 3A). In contrast, the Glencoe 3D survey has an SEG normal polarity, whereby a positive reflection coefficient corresponds to a peak (white) reflection and a negative reflection coefficient is marked by a trough (black) reflection (Fig. 3B). To constrain the age and lithology of mapped reflections, we tied four and five different boreholes to the Chandon and Glencoe 3D surveys, respectively (Fig. 3C). Checkshot data from these boreholes allowed us to establish time-depth relationships for the two seismic surveys (Supplementary Fig. S1; Supplementary Table S1), which we used to depth-convert measurements from TWT to metres. With these time-depth relationships and dominant frequencies of ~40–30 Hz within the interval of interest, we estimate the limits of separability and visibility for both datasets to be ~20±4 m and 3±1 m, respectively. The limit of separability defines the smallest vertical distance between two boundaries for them to be expressed in the data as two individually discrete reflections (e.g., Brown, 2011). At vertical separations less than the limit of separability, the reflected seismic wavelets overlap and undergo tuning associated with either constructive or destructive interference of the two wavelets; this results respectively in either a brightening or dimming of the seismic amplitude. The peaks of the two reflections remain resolvable within the resultant merged wavelet down to a minimum vertical separation at the limit of visibility, at which point it is no longer possible to resolve the two component reflections as separate entities (e.g., Brown, 2011). For any boundaries separated by a vertical distance less than the limit of visibility, their reflection signal is obscured by seismic noise (Brown, 2011). The horizontal resolution within the interval interest, and given the time-depth and frequency ranges, would be equivalent to the bin size, which is ~25 m in both datasets.

3.2. Seismic interpretation

To test the findings of Magee and Jackson (2020b), which focussed on the dyke-induced faults above Dyke E in the Chandon 3D survey, we extend their mapping of 11 seismic horizons (HA–HK; Fig. 3A) to areas above dykes B and D, which are imaged in the Chandon 3D survey. Of these horizons, HK corresponds to the Base Cretaceous unconformity and HF defines the Top Mungaroo Formation (Fig. 3A). The upper tip of some dykes we analyse are deeper than that of Dyke E, meaning their overlying dyke-induced faults extend to greater depths too; we thus also map several horizons below HA (i.e. HAZ–HAW; Fig. 3A). Where possible within the Glencoe 3D survey, we map the same HK–HA horizons above dykes B, D, and E (Fig. 3B). However, due to variations in data quality and reflection continuity within the Glencoe volume, we cannot map horizon HE and instead interpret a deeper reflection we name HD-E (Fig. 3B). In the Glencoe volume we also map an extra horizon, HA-B, between HA and HB (Fig. 3B)

Using transects oriented perpendicular to fault strike and dyke trend, we measure the hanging wall and footwall cut-off pairs for each horizon, where they intersect the studied dyke-induced faults, and the upper tips of underlying dykes (e.g., Fig. 4A). Four of the authors independently mapped fault cut-offs and dyke tips along the same selected graben (Craig Magee = CM; Victoria Love = VL; Karima Fayez = KF; Billy Andrews = BA); this approach allows us to assess the impact of interpretation bias on our findings. Transect spacing is 100 m for BA and 125 m for CM, VL, and KF.

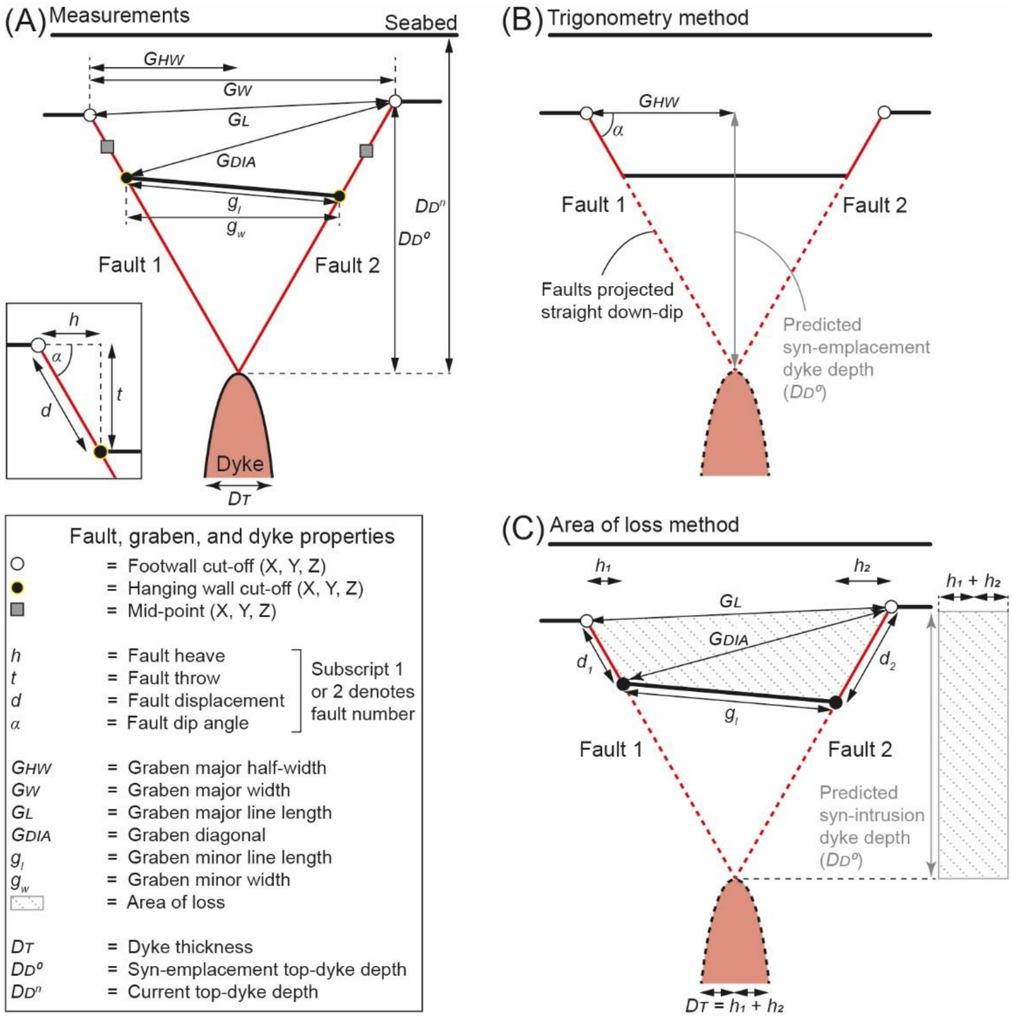

Figure 4: (A) Schematic diagram depicting the different dyke-induced fault and graben properties calculated from the X, Y, and Z co-ordinates of mapped fault-cut-offs. (B) Sketch showing how fault dips and graben half-widths can be used to project faults down-dip and estimate dyke upper tip depths. (C) Sketch showing the graben area of loss and cumulative fault heave (h1 + h2) can be used to define a rectangle, the length of which can be considered equivalent to the dyke upper tip depth (modified from Rivas-Dorado et al., 2021).

3.3. Measurements and calculations

From the coordinates of each interpreted fault cut-off pair, including those mapped by Magee and Jackson (2020b), we calculate fault throw (*t*) and heave (*h*) (Fig. 4A). These throw and heave calculations allow us to estimate fault dip (α) and displacement (*d*), assuming the slip vector is dip-parallel (Fig. 4A) (Magee & Jackson, 2020b). We project displacement data onto fault surfaces at X, Y, and Z coordinates marking the mid-point between each paired footwall and hanging wall cut-off (Fig. 4A); a convergent interpolation gridding algorithm was used to linearly extrapolate between data points and preserve any trends. For fault cut-offs mapped on faults along the same horizon and transect, we combine fault property measurements to derive cumulative throw, heave, and displacement values, as well as the average fault dip (α_{av}). Along each transect, we also use fault cut-off coordinates to calculate (Fig. 4A): (1) the horizontal graben width (G_W) and half-width (G_{HW}) between footwall cut-offs; (2) the line length (G_L) between footwall cut-offs, which unlike G_W or G_{HW} accounts for differences in cut-off elevation; (3) the horizontal graben width (g_w) between hanging wall cut-offs; (4) the line length (g_l) between the hanging wall cut-offs; and (5) the diagonal line length (G_{DIA}) between one hanging wall cut-off and the opposing footwall cut-off.

We apply two methods to predict the current (D_D^n) and syn-emplacement (D_D^0) top-dyke depths from calculated graben width properties (Fig. 4). We first use trigonometry to estimate top-dyke depths from graben half-widths (G_{HW}) and fault dips (α) measured at any stratigraphic level, such as the syn-emplacement free surface (Fig. 4B) (e.g., Pollard et al., 1983, Trippanera et al., 2015b). This trigonometric method assumes faults are planar and project straight down-dip (Fig. 4B) (Magee & Jackson, 2020b). Most studies assume α is constant for both faults and, based on measurements and/or regional information, is ~70–60° (e.g., Rubin & Pollard, 1988, Trippanera et al., 2015a). We present results where we consider that both faults have dips equivalent to either: (1) the average of the two fault dips (α_{av}); (2) 60°, as this is thought typical of normal faults within an Andersonian framework (Anderson, 1951); and (3) 45°, which is similar to the dip of Late Jurassic-to-Early Cretaceous tectonic normal faults in the region (e.g., Magee et al., 2016). We henceforth refer to these three method variants as trigα_{av}, trig60, and trig45, respectively.

In addition to the trigonometry method for predicting top-dyke depths, we use an area of loss method modified from Rivas-Dorado et al. (2021). This method calculates the area between the four fault cut-offs on each transect, which typically define an irregular quadrilateral shape, and creates a rectangle of the same area (Fig. 4C) (Rivas-Dorado et al., 2021). By setting the width of this derived rectangle to equal the cumulative fault heave, which is assumed equivalent to dyke thickness (D_T), the resulting length of the rectangle is taken as the vertical distance between the syn-emplacement surface and dyke upper tip (Fig. 4C); i.e. the graben area of loss is assumed to equal the area gained by dyke-driven extension (Rivas-

Dorado et al., 2021). Our methodology for finding the area of loss accounts for all cut-offs occurring at different elevations/depths, as opposed to the hanging wall cut-offs being assumed to have the same elevation (Rivas-Dorado et al., 2021).

3.4. Limitations and errors

Although seismic reflection data provide unique insight into the 3D structure of dykes and dyke-induced faults, interpreting and quantitatively assessing these features, which often have displacements of <20 m, is affected by several objective and subjective uncertainties involved in seismic interpretation (e.g., Dimmen et al., 2022, Magee & Jackson, 2020b, Wilson et al., 2019). Objective uncertainty, which can often be quantified, includes limitations related to resolution and quality of seismic imaging, as well as seismic velocities used for depth conversion (Faleide et al., 2021). For example, the seismic velocities we use are taken from borehole data, meaning they do not capture possible variations in seismic velocity across the study area, away from the borehole locations (Magee & Jackson, 2020b). However, because the time-depth relationships of the boreholes for each 3D survey we use are similar (Supplementary Fig. 1), we adopt the conservative view that calculated seismic velocities could vary by up to ±10% (Magee & Jackson, 2020a, Magee & Jackson, 2020b).

It is also important to consider that the dykes and dyke-induced faults in the Exmouth Plateau formed during the Late Jurassic, and have since been buried by several kilometres of sedimentary strata (Magee & Jackson, 2020a). Most sedimentary rocks compact as they are buried, reducing stratal thicknesses and rotating any pre-existing, inclined fractures to shallower angles (Allen & Allen, 2013). Burial-related compaction can thus reduce fault throw, potentially by up to 15% in sand-dominated or mixed sand-shale lithologies (Taylor et al., 2008), meaning our calculated fault dips, displacements, and predicted top-dyke depths are minimum estimates. However, we note that all dykes and dyke-induced faults occur at similar depths (~3–4 km) under a similar overburden thickness, so we suggest compaction, and compaction-related modification of the primary geometries, can be considered to have been constant across the study area (Magee & Jackson, 2020a, Magee & Jackson, 2020b). Although our measurements and calculations may not therefore reflect the absolute syn-emplacement 3D structure of the dyke and dyke-induced faults, their relative values will be comparable, i.e. the current patterns of displacement, dip, or predicted dyke upper tip depth distribution will be the same as when dyking occurred in the Late Jurassic.

Subjective uncertainties and biases relate to those introduced by the person undertaking the interpretation and are generally more difficult to quantify (e.g., Alcalde et al., 2017a, Bond et al., 2007, Faleide et al., 2021, Wilson et al., 2019). For example, mapping footwall and hanging wall cut-offs of low offset faults, or faults with a high proportion of continuous deformation, is particularly prone to interpretation bias (Schaaf & Bond, 2019). Where fault displacement is substantially greater than the limit of separability and horizontal resolution, reflections are often clearly offset and discrete footwall and hanging wall cut-offs can be identified (Figs 5A and B) (Dimmen et al., 2022). In these cases, any fault-related continuous deformation (i.e. local rotation of bedding and thus reflections adjacent to faults; Delogkos et al., 2017) can be accounted for by projecting the regional dip of horizons onto the fault to define cut-off positions (Figs 5A and C) (e.g., Mansfield & Cartwright, 1996). In contrast, where fault displacement is close to or below the limit of separability and horizontal resolution, reflections are continuous but appear locally distorted (Figs 5A and D) (e.g., Dimmen et al., 2022, Faleide et al., 2021). Here, it is the interpreter's decision, which can be biased by experience (e.g., Bond et al., 2007), as to where to place the footwall and hanging wall cut-offs (Fig. 5D). For example, an interpreted portion of the fault will have a shallower dip and larger displacement (and heave) if cut-offs are mapped at the inflection points of a distorted reflection, as opposed to projecting the cut-offs to a mid-point (Fig. 5D). Any projection of cut-offs also influences measured graben width properties. Given limitations of data resolution and imaging quality, there is no unique, or 'correct', interpretation of fault cut-off location (e.g., Alcalde et al., 2017a, Dimmen et al., 2022, Faleide et al., 2021).

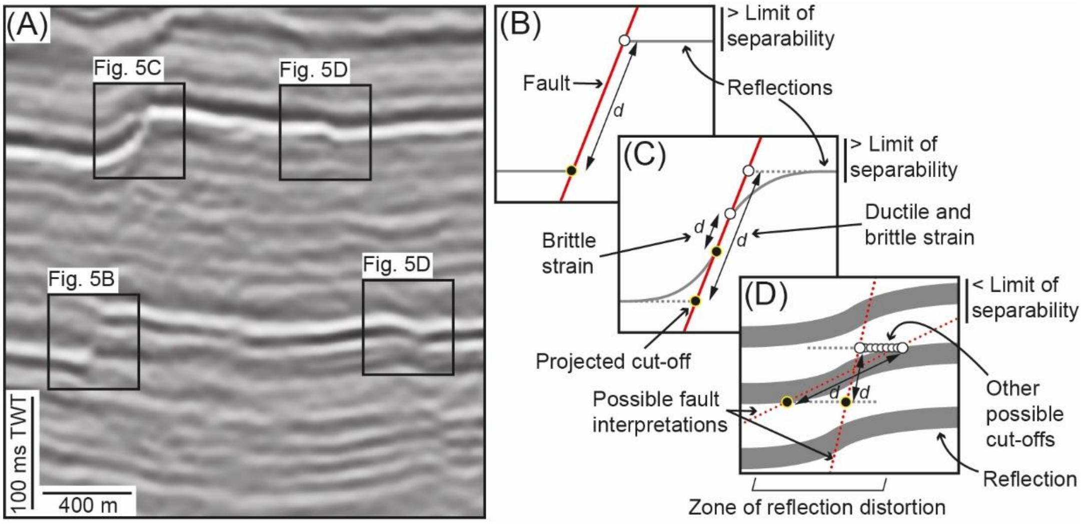

Figure 5: (A) Uninterpreted seismic section from the Chandon 3D survey showing different reflection configurations across two faults. (B-D) Schematic diagrams describing how and where fault footwall and hanging wall cut-offs may be interpreted for the different reflection-fault interactions in (A) (e.g., Dimmen et al., 2022).

Previous studies have suggested interpretation bias in quantifying dyke-induced fault properties can be conservatively accounted for by applying ±5% measurement errors (Magee & Jackson, 2020b). To preliminarily explore the effect of interpretation bias, and test these prior assumptions, we present data based on independent mapping of fault cut-offs by four individuals (CM = Craig Magee; VL = Victoria Love; KF = Karima Fayez; BA = Billy Andrews). Each interpreter mapped fault cut-offs along the Top Mungaroo Formation for one or several dyke-induced fault pairs, using different transects and transect spacings relative to others. We also conducted a repeat experiment whereby CM mapped dyke-induced fault cut-offs above Dyke D along the Top Mungaroo Formation on the same transects on two occasions (CM1 and CM2), separated by ~1 year. To compare the results from these interpreter datasets, we use F-tests to statistically determine the probability that calculated fault properties or predicted dyke upper tip depths are not significantly different. If the calculated F value for the two or three datasets being compared is less than a critical amount (F_{crit}), the null hypothesis that the datasets may be considered equal is accepted.

4. Results

4.1. Structural framework

For all dykes, their associated dyke-induced faults are sub-parallel to the dyke strike (Fig. 3C). Dykes D and E are sub-parallel and strike ~012° (Fig. 3C). Dyke B and its dyke-induced faults trend ~002°, intersecting other dykes (i.e. C, D, and E) and associated faults, respectively (Fig. 3C). Where these dykes and faults intersect, they can be difficult to identify and assign (Fig. 3C). Dyke B and its dyke-induced faults also cross-cut or are cross-cut by a major W-dipping, ~N-S striking, tectonic normal fault, and several smaller associated tectonic faults within the Chandon 3D survey (Fig. 3C). Within the Chandon 3D survey, dyke-induced faults above Dyke D are also cross-cut, and possibly offset by, a minor S-dipping, ~NW-SE striking, tectonic normal fault (Fig. 3C). Elsewhere in the study area, there is little connectivity between the studied dyke-induced faults and tectonic faults (Fig. 3C).

4.2. Dyke D and its overlying dyke-induced faults

To illustrate our research methodology, we first present quantitative data from the dyke-induced faults, which we separate into DF1-DF2 and DF3-DF4 pairs, above Dyke D in the Chandon 3D survey (Fig. 6A). We start by analysing graben width, average fault dip, and cumulative fault displacement along DF1-DF2 and DF3-DF4 at the Top Mungaroo Formation (horizon HF) (Fig. 6). To calculate these data, CM and BA interpret footwall and hanging wall cut-offs on different seismic sections spaced 125 m or 100 m apart, respectively (Fig. 6A); two cut-off sets are mapped by CM (i.e. CM1 and CM2; Fig. 6). These data allow us to predict Dyke D top-dyke depths, which we compare to top-dyke depths measured from the seismic reflection data. Finally, we demonstrate how graben width measurements collected along different stratigraphic horizon improve top-dyke depth predictions.

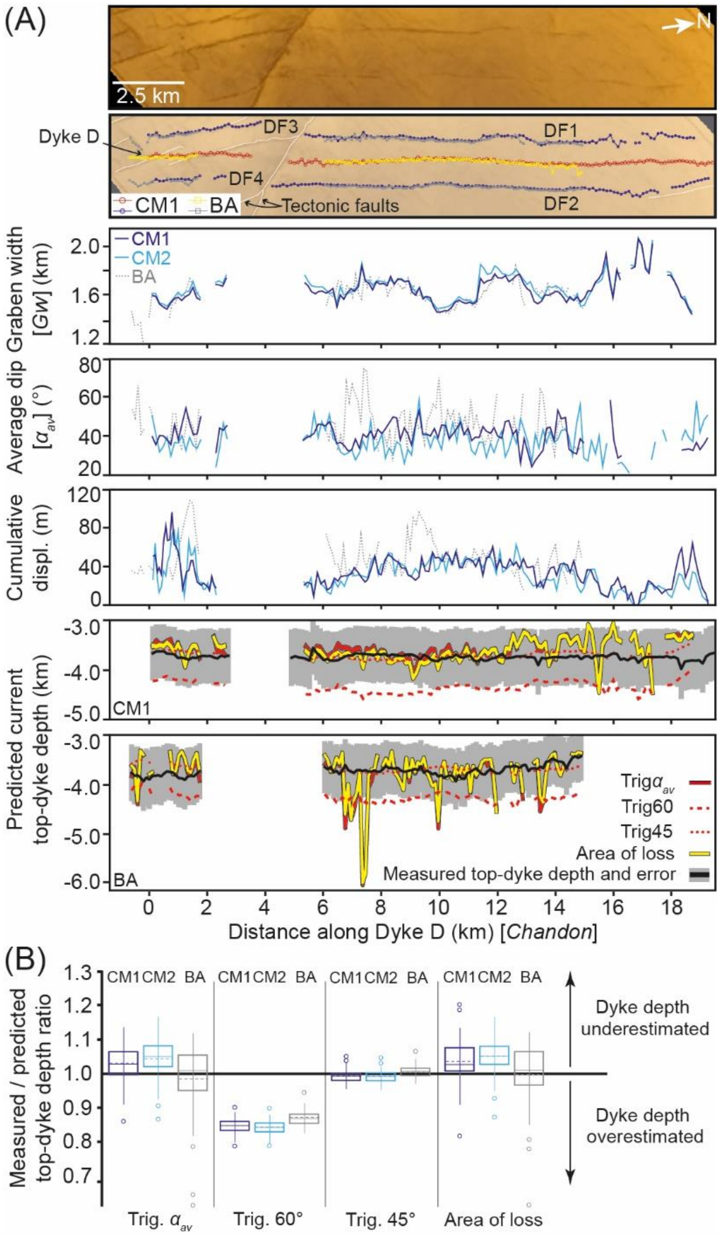

Figure 6: (A) Uninterpreted and interpreted time-structure map of the Top Mungaroo Formation (horizon HF) above Dyke D in the Chandon 3D survey (see Fig. 3C for key and location). Footwall cut-off and dyke upper tip depth locations mapped by CM1 and BA are shown. Plots compare graben width, average fault dip, and cumulative displacement (displ.) calculated from CM1, CM2, and BA cut-off mapping. Also shown are plots comparing measured top-dyke depths with those predicted by CM1 and BA using different methods (trigαav, trig60, trig 45, and area of loss). Error bars are not shown because we compare calculations subject to the same uncertainties and to improve clarity; we make an exception for the measured top-dyke depths, for which we include a ±15% error envelope, to enable a broader comparison to predicted top-dyke depths. (B) Box-and-whisker plots comparing measured and predicted top-dyke depth ratios calculated by different methods and using fault cut-off datasets mapped by

different interpreters (CM1, CM2, and BA). The boxes describe the interquartile range and median of each dataset, with the whiskers marking lower and upper extremes of the data. We also show the mean (dashed line) and outliers in these data.

Above Dyke D along the Top Mungaroo Formation, graben widths are ~1.20–2.05 km, average fault dips are ~20–85°, and cumulative displacements are ~5–97 m (Fig. 6; Supplementary Table S2). Dyke-induced fault lengths mapped by CM and BA differ, with CM interpreting DF1-DF2 ~3 km further northwards than BA (Fig. 6A). Where fault cut-offs interpreted by CM and BA spatially overlap, graben widths are similar, displaying systematic increases and decreases along-strike at the kilometre-scale (Fig. 6A). The average fault dips and cumulative displacement calculated by CM1, CM2, and BA are more variable (Fig. 6A; Supplementary Table S2). Differences between the CM1 and CM2 datasets, which use the same transects, are due to small offsets of ≲100 m in cut-off positions (average is ~18 m; Supplementary Table S3) but statistical F-tests reveal their variance is insignificant (i.e. $F<F_{crit}$; Table 1); i.e. the CM1 and CM2 datasets may be considered equal. Conversely, F-tests demonstrate that variances between the CM1, CM2, and BA measurements of graben width, average fault dip, and cumulative displacement are significant (i.e. $F>F_{crit}$; Table 1); i.e. the null hypothesis can thus be rejected and the CM and BA datasets considered unequal.

Table 1: Statistical F-tests comparing CM1, CM2, and BA data

Property	Interpreter	Mean	Variance	CM1 and CM2 comparison		CM1, CM2, and BA comparison	
		(m)		F	F_{crit}	F	F_{crit}
Horizontal graben width [G_W]	CM1	1658	011843				
	CM2	1679	011904	1.01	1.35	14.58	3.02
	BA	1602	010577				
Average fault dip [α_{av}]	CM1	0040	000038				
	CM2	0037	000052	1.36	1.37	35.78	3.02
	BA	0046	000102				
Cumulative displacement	CM1	0036	000167				
	CM2	0034	000225	1.35	1.35	31.87	3.02
	BA	0050	000365				
Trigα_{av} estimated top-dyke depth	CM1	3556	029921				
	CM2	3501	030500	1.02	1.37	26.45	3.02
	BA	3778	205831				
Trig60 estimated current top-dyke depth	CM1	4282	008973				
	CM2	4300	009292	1.04	1.35	08.98	3.02
	BA	4246	008696				
Trig45 estimated current top-dyke depth	CM1	3675	003510				
	CM2	3686	003649	1.04	1.35	05.23	3.02
	BA	3660	003217				
Area of loss estimated current top-dyke-depth	CM1	3547	040773				
	CM2	3488	027126	1.50	1.35	21.90	3.02
	BA	3735	197886				

Measured top-dyke depths for Dyke D in the Chandon 3D survey range from ~3.5–3.8 km beneath current sea-level (Supplementary Table S2), which broadly correspond to emplacement depths of ~0.9–1.1 km beneath the syn-intrusion surface, Horizon HK (Fig. 6A). Along the graben, over lateral distances of ~125–250 m, there are some abrupt changes of up to ~200 m in measured top-dyke depth superimposed onto subtle (<100 m) increases and decreases over the kilometre-scale (Fig. 6A). Predictions of current top-dyke depths derived using the trigα_{av}, trig45, and area of loss methods are often within error of measured top-dyke depths for both CM and BA (Fig. 6; Supplementary Table S2). However, top-dyke depths predicted using the trig60 method appear to overestimate dyke depths (Fig. 6A). Statistical F-tests reveal the variance of trigα_{av}, trig60, and trig 45 calculations by CM1 and CM2 is insignificant (Table 1). Only for top-dyke depths predicted using the area of loss method is the variance significant, F (1.50) > F_{crit} (1.35), indicating the CM1 and CM2 calculations are unequal (Table 1). F-tests demonstrate the CM and BA top-dyke depth estimates are unequal, regardless of the prediction method used (Table 1).

We also measure graben width and predict top-dyke depths using fault cut-offs for DF1-DF2 and DF3-DF4 mapped at various stratigraphic horizons (e.g., Fig. 7). As part of the CM1 analysis, we show graben width is variable along DF1-DF2 and DF3-DF4 at all stratigraphic levels and decreases with depth

(Fig. 7A) (data provided in Magee & Love, 2021). Top-dyke depths, relative to current sea-level, predicted from these graben width measurements at different stratigraphic levels do vary, but together define a mean profile with relatively low standard deviations of ≲300 m (e.g., Figs 7B and C). Comparing the mean top-dyke depth estimates with those measured from the seismic reflection data reveals that: (1) predictions derived from the trigα_{av}, trig45, and area of loss methods are broadly comparable to measured top-dyke depths, although on average they underestimate top-dyke depths by ≲170 m; and (2) the trig60 predictions are now within the error of measured top-dyke depths, but overestimate measured values by ~420 m (Fig. 7D).

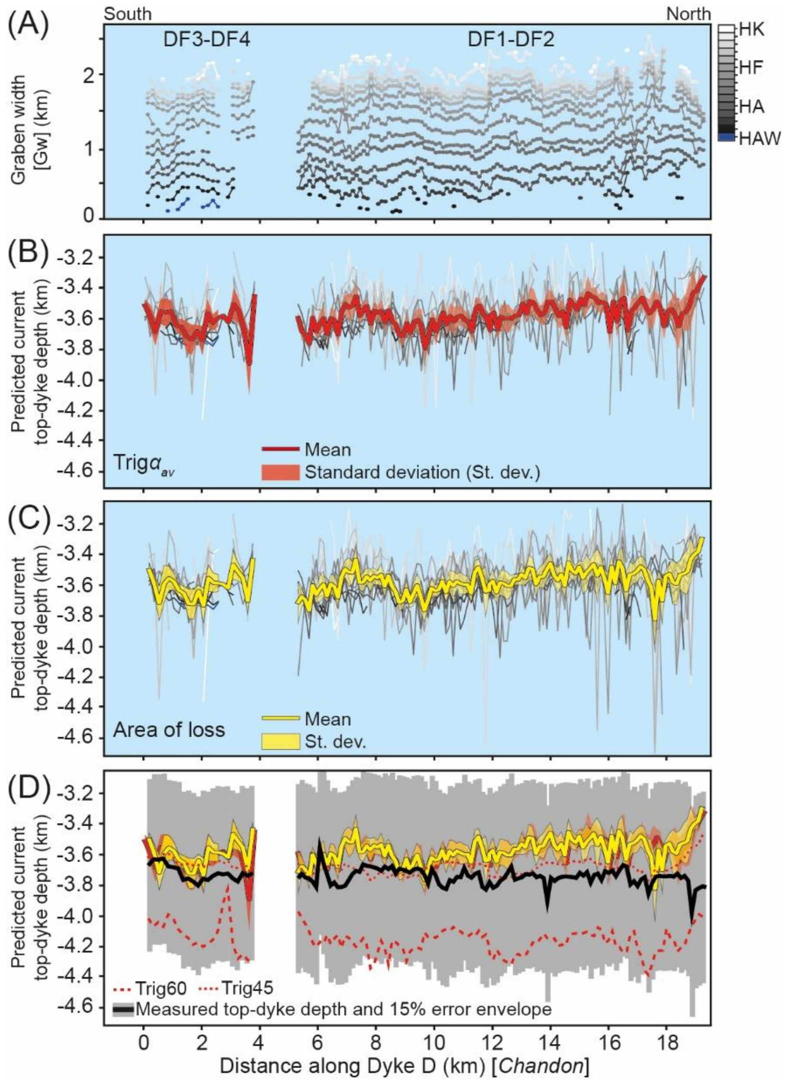

Figure 7: (A) Graben width measurements for horizons HK–HAW above Dyke D in the Chandon 3D survey. Error bars not shown for clarity. (B) Top-dyke depths predicted using graben widths and average fault dips acquired from each horizon (HK–HAW) on each measurement transect. From the predicted

top-dyke depths for all horizons, we calculate their mean and standard deviation. (C) Top-dyke depths predicted using the area of loss method and fault cut-offs mapped for each horizon (HK–HAW) on each measurement transect. From the predicted top-dyke depths for all horizons, we calculate their mean and standard deviation. (D) Plot comparing measured top-dyke depths with mean predicted top-dyke depths estimated using different methods (trigαav, trig60, trig 45, and area of loss). Standard deviation envelopes are shown for the trigαav and area of loss methods.

4.3. Graben widths along the Top Mungaroo Formation and predicted top-dyke depths

To further test how interpreter bias may influence quantitative dyke-induced fault analyses, we examine how graben width measurements and predicted top-dyke depths for dykes B and E vary between three interpreters (i.e. CM, VL, and KF; Fig. 8) (all data available in Magee, 2022, Magee & Love, 2021). For this analysis, we split the dyke-induced faults traces above Dyke B in the Chandon 3D survey into sections (Fig. 8B): (1) faults BF1a and BF1b both dip eastwards and overlap laterally by ~700 m towards their upper tips, but are otherwise hard-linked and occur opposite BF2a; (2) further north, the merging of faults above dykes B and C make it difficult to accurately map their continuation, so we define faults BCF1 and BCF2 separately; and (3) north of where dykes B and C link, we map dyke-induced faults BF1c and BF2a. The Dyke B dyke-induced faults analysed within the Glencoe 3D survey are labelled BF3-BF4 (Fig. 8A). The Dyke E dyke-induced faults in the Chandon 3D survey are named EF1-EF2 (Magee & Jackson, 2020b) and EF3-EF4 in the Glencoe 3D survey (Figs 8C and D).

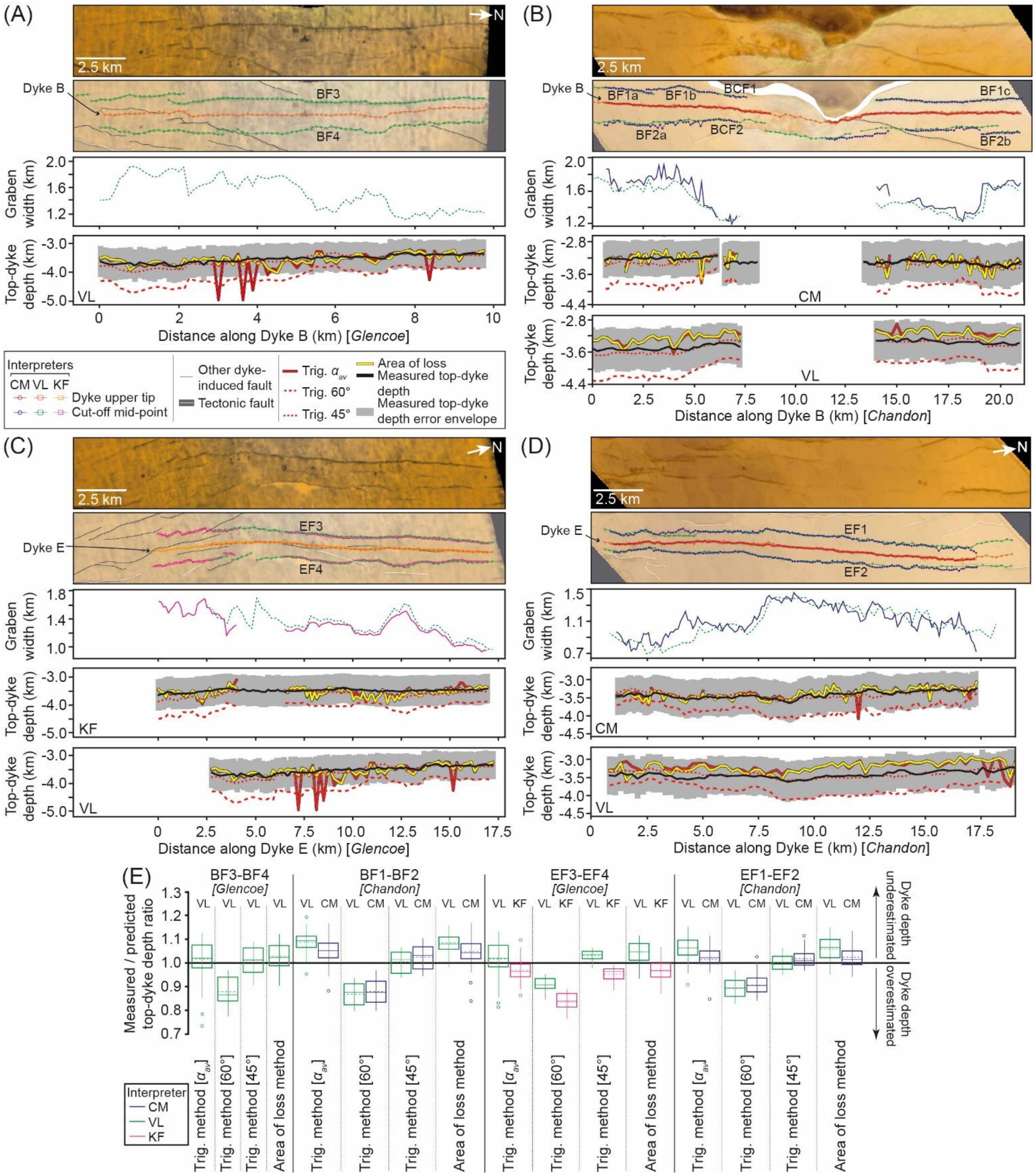

Figure 8: (A-D) Uninterpreted and interpreted time-structure maps of the Top Mungaroo Formation (horizon HF) above dyke B and E in the Chandon and Glencoe 3D surveys (see Fig. 3C for key and locations). Footwall cut-off and dyke upper tip depth locations mapped by different interpreters are shown. Plots compare graben width, average fault dip, and cumulative displacement (displ.) calculated from different interpreters' cut-off mapping. Also shown are plots comparing measured top-dyke depths with those predicted using different methods (trigαav, trig60, trig 45, and area of loss). Error bars are

not shown because we compare calculations subject to the same uncertainties and to improve clarity; we make an exception for the measured top-dyke depths, for which we include a ±15% error envelope, to enable a broader comparison to predicted top-dyke depths. (E) Box-and-whisker plots comparing measured and predicted top-dyke depths ratios calculated by different methods and using fault cut-off datasets mapped by different interpreters. The boxes describe the interquartile range and median of each dataset, with the whiskers marking lower and upper extremes of the data. We also show the mean (dashed line) and outliers in these data.

Across the Top Mungaroo Formation (Horizon HF), we observe both gradual changes along-strike in graben width (e.g., EF1-EF2; Fig. 8D), and abrupt changes where overlapping fault segments occur (e.g., BF3-BF4; Fig. 8A). Most measurements of graben width at the Top Mungaroo Formation are similar (i.e. <100 m difference) but can vary by up to ~400 m (Figs 8B-E). Comparing measured top-dyke depths and those predicted using the graben widths measured along the Top Mungaroo Formation above of dykes B and E reveals that (Fig. 8): (1) predicted top-dyke depths derived from the trigα_{av}, trig45, and area of loss methods are broadly comparable to measured top-dyke depths; (2) top-dyke depth predictions calculated using the trig60 method overestimates measured top-dyke depths; (3) even though the four interpreters mapped fault cut-offs on different transects, there is generally good agreement in their predicted top-dyke depths, except for EF3-EF4; (4) top-dyke depths appear to increase and decrease by ~100 m over several kilometres; and (5) abrupt and isolated changes in predicted top-dyke depths along individual graben occur when calculated using the trigα_{av} and area of loss methods, but are absent when fault dip is assumed to be 60° or 45°. Statistical F-tests reveal that the variance between graben width measurements acquired by different interpreters above the same fault are not significant and may thus be considered equal (i.e. $F<F_{crit}$; Table 2). We also show that variance between top-dyke depth predictions for Dyke E in the Chandon 3D survey is insignificant may be considered equal, regardless of the interpreter or prediction method, but for the Glencoe 3D survey most interpreter predictions are significantly different from each other, except where the area of loss method was employed (Table 2). For Dyke B in the Chandon 3D

survey, the trig60 and trig45 top-dyke depth predictions calculated from CM and VL interpretations may be considered equal, but the trigα_{av} and area of loss data unequal (Table 2).

Table 2: Statistical F-tests comparing CM, VL, and KF data

Dyke-induced graben	Property	Interpreter	Mean (m)	Variance	F	F_{crit}
Dyke B, Chandon 3D survey	Horizontal graben width [G_W]	CM	1561	35490	1.31	1.49
		VL	1489	27083		
	Trigα_{av} estimated top-dyke depth	CM	3386	28122	1.65	1.49
		VL	3183	16996		
	Trig60 estimated current top-dyke depth	CM	4044	47071	1.14	1.49
		VL	3988	41204		
	Trig45 estimated current top-dyke depth	CM	3473	23542	1.08	1.49
		VL	3443	21842		
	Area of loss estimated current top-dyke-depth	CM	3403	32538	2.05	1.49
		VL	3198	15896		
Dyke E, Chandon 3D survey	Horizontal graben width [G_W]	CM	1120	30234	1.30	1.38
		VL	1102	39193		
	Trigα_{av} estimated top-dyke depth	CM	3379	17325	1.14	1.39
		VL	3205	19709		
	Trig60 estimated current top-dyke depth	CM	3818	23523	1.14	1.38
		VL	3803	26909		
	Trig45 estimated current top-dyke depth	CM	3408	09373	1.04	1.38
		VL	3400	09740		
	Area of loss estimated current top-dyke-depth	CM	3389	17627	1.24	1.38
		VL	3214	21813		
Dyke E, Glencoe 3D survey	Horizontal graben width [G_W]	KF	1303	34003	1.22	1.48
		VL	1321	27901		
	Trigα_{av} estimated top-dyke depth	KF	3520	21619	3.58	1.44
		VL	3618	77428		
	Trig60 estimated current top-dyke depth	KF	4056	26940	1.87	1.48
		VL	4031	14413		
	Trig45 estimated current top-dyke depth	KF	3579	10988	2.17	1.48
		VL	3548	05053		
	Area of loss estimated current top-dyke-depth	KF	3509	19878	1.01	1.44
		VL	3535	19741		

4.4. Graben widths and predicted top-dyke depths in 3D

To better evaluate the validity of top-dyke depth prediction methods, and extend the 3D analysis of DF1-DF2 and DF3-DF4 (Fig. 7), we measured graben width across all mapped horizons above Dyke B in the Chandon 3D survey and Dyke E in the Chandon and Glencoe 3D surveys (all data provided in Magee, 2022, Magee & Love, 2021). From these graben width measurements, we estimate the top-dyke depth beneath each horizon (e.g., Figs 7 and 9). The measured top-dyke depths beneath current sea-level range from ~3.3–3.7 km and ~3.3–3.6 km for dykes B and E, respectively (Figs 9A and B). Along the graben, over lateral distances of ~125–250 m, there are some abrupt changes of up to ~100 m in measured top-dyke depth superimposed onto broad increases and decreases of up to ~300 m over the kilometre-scale (Figs 9A and B). By compiling data for all stratigraphic horizons, we show there is no correlation (R^2=0.04) between measured graben widths and measured top-dyke depths (Fig. 9C).

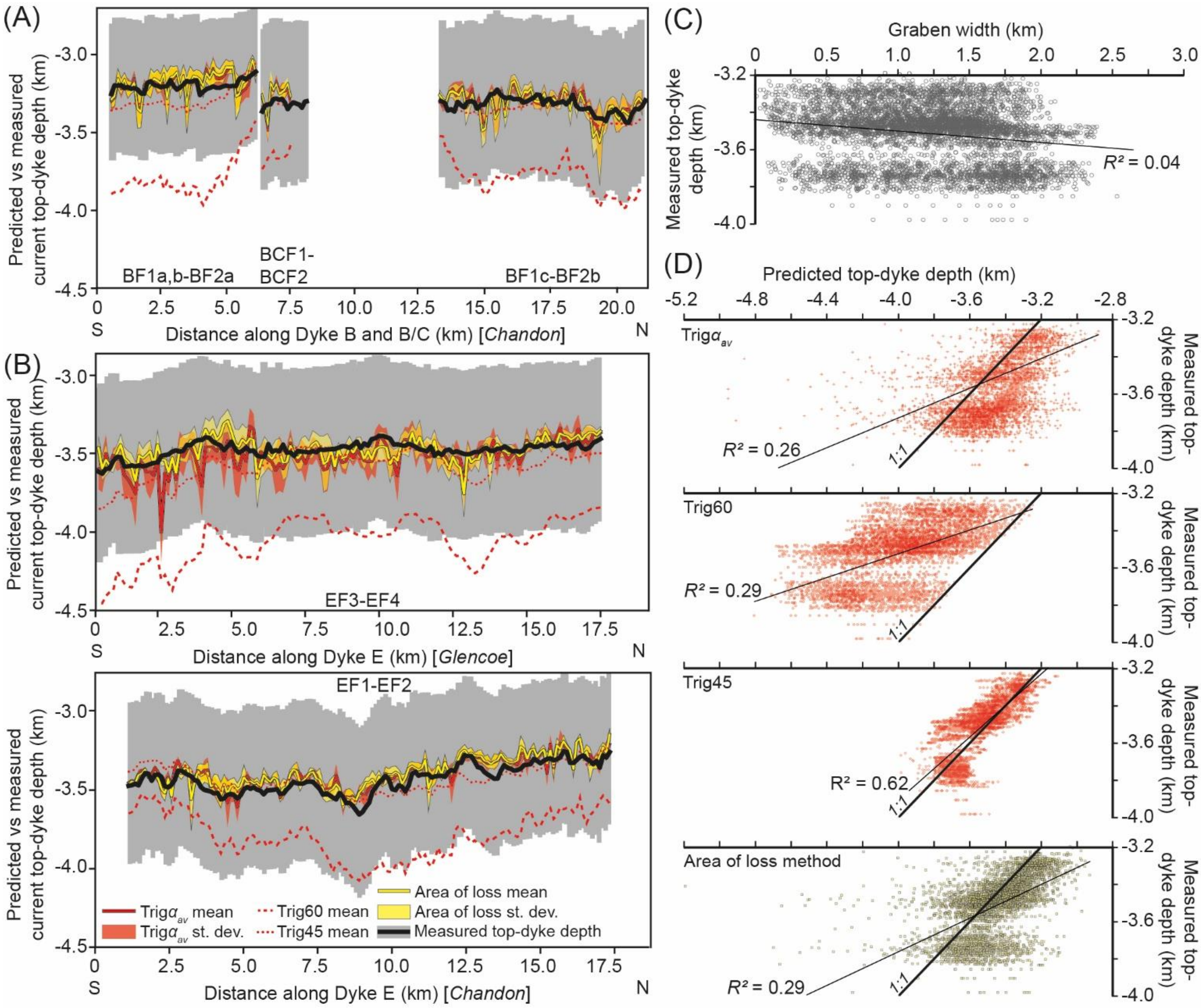

Figure 9: (A-B) Plots comparing measured top-dyke depths with mean predicted top-dyke depths estimated from all horizons using different methods (trigαav, trig60, trig 45, and area of loss) for dykes B and E in the Chandon and Glencoe 3D surveys. Standard deviation envelopes are shown for the trigαav and area of loss methods, and the error envelope (grey) of the measured top-dyke depths is ±15%. (C) Measured graben widths from all horizons compared to underlying top-dyke depths. (D) All

measured top-dyke depths compared to predicted top-dyke depths estimated from the trigαav, trig60, trig 45, and area of loss methods used.

There is often scatter between the predicted top-dyke depths from different horizons, but mean values display relatively low (≲200 m) standard deviations (Figs 9A and B). Like our analysis of predicted top-dyke depths predicted from graben widths along the Top Mungaroo Formation, we show predictions derived from the trigα_{av}, trig45, and area of loss methods appear broadly comparable to measured top-dyke depths (Figs 9A and B). In contrast, top-dyke depths predicted using the trig60 method appear to overestimate dyke depths (Figs 9A and B). If we compare all top-dyke depth predictions, and not just derived means, those calculated using the trigα_{av} and area of loss methods are positively but weakly (R^2=0.26 and 0.29) correlated to measured top-dyke depths; these methods have Root-Mean Square Errors (RSME) of ~180 m and seemingly tend to underestimate top-dyke depths (Fig. 9D). The trig60 method is similarly positively but weakly (R^2=0.29) correlated to measured top-dyke depths, but overestimates top-dyke depths and has an RSME of ~500 m (Fig. 9D). Top-dyke depth predictions derived from the trig45 method display a moderate (R^2=0.62), positive correlation with the measured top-dyke depths, and a RSME of ~100 m (Fig. 9D).

4.5. Fault displacement and dip in 3D

We show how displacement varies along-strike and down-dip of all studied dyke-induced faults (Figs 10A) (all data provided in Magee, 2022, Magee & Love, 2021). Across these dyke-induced faults, displacement has a right-skew distribution but is ~26 m on average with a standard deviation of ~18 m (Fig. 10B). Displacement maxima rarely occur at fault upper or lower tips, with displacement typically higher towards fault centres (Figs 10A and C). Across EF1 and EF2 in the Chandon 3D survey, displacement gradually decreases northwards and is consistently greatest (up to ~101 ± 15 m) on the W-dipping fault (EF2) where three, possibly four, zones of locally elevated displacement can be recognised (Fig. 10A) (see also Magee & Jackson, 2020b). There are no such zones of elevated displacement along EF1 (Fig. 10A). In the Glencoe

Figure 11: (A) Fault dip (α) maps (see Magee & Jackson, 2020b for method). Dyke traces also shown

(Magee & Jackson, 2020a). Fault dip maps may contain interpolation errors derived from our choice gridding algorithms, but we consider these negligible given the high density of measurement locations across both faults. (B) Probability density function plot of measured average fault dips (αav), showing they have a normal distribution. (C) Fault dip compared to the depth of the hanging wall cut-off used in its calculation. 3D survey, it is the E-dipping fault, EF3, which consistently has the greatest displacement (up to ~134 ± 18 m) (Fig. 10A). Yet EF3 shows no clear zones of elevated displacement, whereas EF4 can be sub-divided into at least three zones (Fig. 10A). Where zones of elevated displacement occur along EF2 and EF4, they broadly appear to correlate with areas of higher fault dip (Fig. 10). For the dyke-induced faults above dykes B and D, displacement gradually decreases northwards but there are no obvious zones of locally elevated displacement (Fig. 10A). The dyke-induced faults above Dyke D have lower displacement (up to ~65 ± 10 m) than those above dykes B (up to ~173 ± 26 m) and E (Fig. 10A). There is not statistical correlation between measured top-dyke depths and maximum displacements measured on each horizon at each transect, but there is a hint that dyke-induced faults accrue more displacement when dykes reach shallower levels (Fig. 10D).

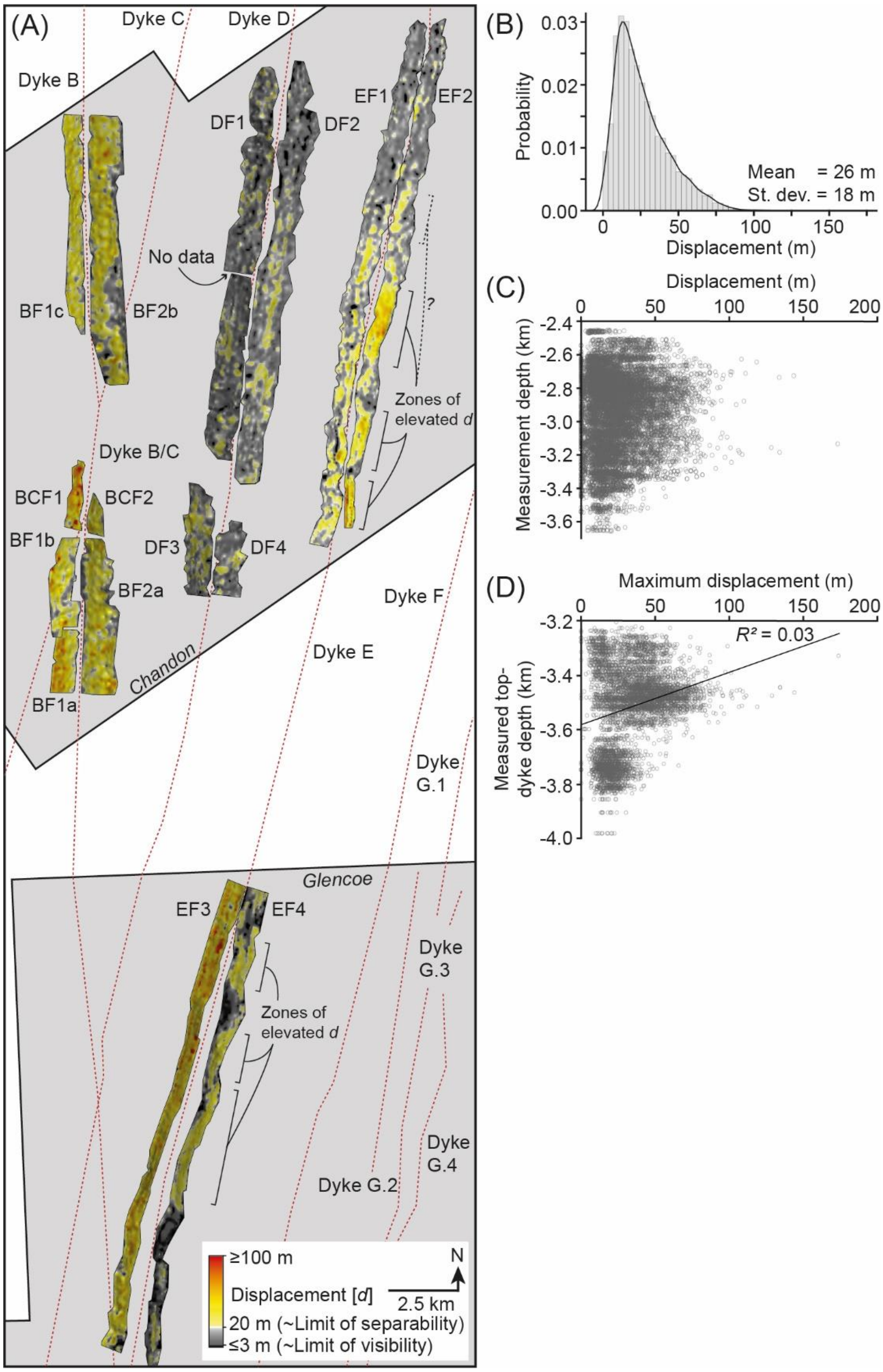

Figure 10: (A) Fault displacement maps (see Magee & Jackson, 2020b for method). Dyke traces also shown (Magee & Jackson, 2020a). Fault displacement maps may contain interpolation errors derived from our choice gridding algorithms, but we consider these negligible given the high density of measurement locations across both faults. (B) Probability density function plot of measured fault displacements, showing they have a right-skewed distribution. (C) Fault displacement compared to the depth of the hanging wall cut-off used in its calculation. (D) Maximum displacement of the two

opposing dyke-induced faults on each measurement transect at each horizon, compared to the measured underlying top-dyke depth.

We show dip varies along-strike and down-dip of all studied dyke-induced faults, although there are no systematic changes in its distribution (Figs 11A). Average fault dips, calculated from the dips of both opposing dyke-induced faults on each transect at each horizon, are normally distributed with a mean of 41° and standard deviation of 7.5° (Fig. 11B). There is no systematic change in average fault dip with depth (Fig. 11C).

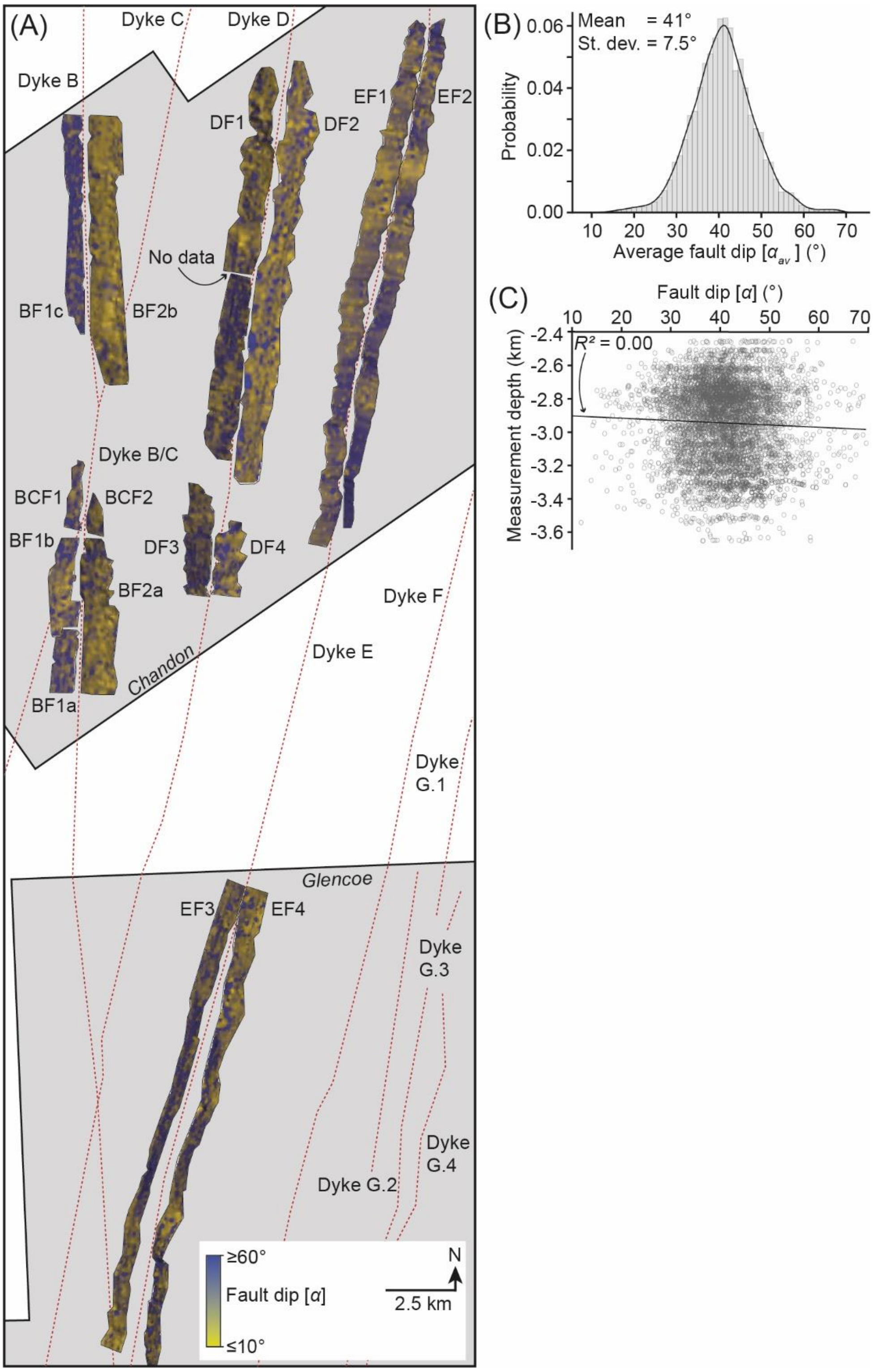

Figure 11: (A) Fault dip (α) maps (see Magee & Jackson, 2020b for method). Dyke traces also shown (Magee & Jackson, 2020a). Fault dip maps may contain interpolation errors derived from our choice gridding algorithms, but we consider these negligible given the high density of measurement locations across both faults. (B) Probability density function plot of measured average fault dips (αav), showing they have a normal distribution. (C) Fault dip compared to the depth of the hanging wall cut-off used in its calculation.

5. Discussion

5.1. Interpretation bias

The studied dyke-induced faults have relatively low displacements (typically <75 m, with an average of ~26 m; Fig. 10B). Given the vertical (~20 ± 4 m) and horizontal (~25 m) resolution limits of the seismic reflection data used, these low displacements mean many portions of the dyke-induced faults are not imaged as clear offsets in reflections (e.g., Fig. 5i). Instead, the dyke-induced faults often correspond to areas where seismic reflections are subtly distorted and appear folded (e.g., Figs 3A, B, and 5iii). In such a situation, a dyke-induced fault may extend through the distorted reflections, but the interpreter has to decide whether the fault intersects the middle of the rotated reflection limb, either of its inflection points, or elsewhere (e.g., Fig. 5iii) (e.g., Faleide et al., 2021). It is also plausible that the distorted reflections correspond to folded strata, perhaps generated by fault propagation folding above a buried fault tip, and there is no fault present at that stratigraphic level at all. These uncertainties, associated with mapping fault cut-offs, affect all quantitative fault measurements (e.g., displacement and graben width) (e.g., Alcalde et al., 2017a, Faleide et al., 2021). In their quantitative dyke-induced fault study, Magee and Jackson (2020b) assumed this interpreter bias could be accounted for by considering measured or calculated fault properties had errors of ± 5%.

In our study, where the same fault cut-off sets were mapped by the same interpreter, but at a different time (i.e. CM1 and CM2), variations in average dip and cumulative displacement occur due to supposedly coincident fault cut-offs being mapped up to ~100 m along-strike (~18 m on average) (Supplementary Table S3). These distances have the same order of magnitude as fault heave and throw, and therefore significantly affect calculated dips and displacements. Conversely, the ≲100 m differences in fault cut-off position are much less than, and thus have little impact on graben widths (>1500 m; Supplementary Table S2). Despite these differences in fault cut-off position, our statistical F-test confirm little variance between fault properties extracted from the two compared datasets (i.e. CM1 and CM2), indicating they can be considered equal (Table 1). Additionally, top-dyke depths predicted from both datasets using trigonometry methods are statistically equal; however, those predicted using the area of loss method are unequal (Table 1). Our data thus suggest that although an individual interpreter may introduce bias into their fault cut-off mapping, their findings are generally consistent. Such 'internal consistency' from geologists has been observed for several data types, including the characterisation of faults and fractures (Andrews et al., 2019, Shipton et al., 2020) and models built from seismic reflection datasets (Alcalde & Bond, 2022); this is likely a result of the mental model(s) of the interpreter (i.e. the simplified internal representation of the process or problem being assessed) (e.g., Gibson et al., 2016, Shipley & Tikoff, 2016). These mental models are influenced by the cogitative style and experience of the interpreter (Bond et al., 2007, Shipley & Tikoff, 2016), as well as the purpose and time constraints associated with data collection and quality control (e.g., Shipton et al., 2020).

In our study, where fault properties and predicted top-dyke depths are derived from fault cut-offs mapped by *different* interpreters, their values are broadly similar and the same profile patterns along the graben length are reproduced (Figs 6 and 8). Our statistical F-test shows that, in some instances, fault properties and predicted top-dyke depths can be considered equal, but not always (Tables 1 and 2). There are many potential reasons why data derived from different interpreters is variable, including: (1) seismic reflection data quality (Alcalde et al., 2017a, Alcalde et al., 2017b, Faleide et al., 2021); (2) interpreter experience (Bond et al., 2007, Bond et al., 2015); (3) applied methods of mapping (e.g., were seismic attributes used to constrain interpretations?) (Rankey & Mitchell, 2003); (4) the vertical exaggeration and scale used during fault picking (Alcalde et al., 2019); and (5) the time available to collect and quality check the dataset (e.g., Bond et al., 2007, Bond et al., 2015, Faleide et al., 2021, Macrae et al., 2016). Previous work has shown that variance between interpreters can be reduced where a pre-interpretation picking strategy was implemented, training material was used by all interpreters prior to picking, and/or an element of group working or training is employed (see Alcalde & Bond, 2022 and references therin). Overall, our data suggest that the arbitrary 5% error applied by Magee and Jackson (2020b) may be insufficient to describe extracted fault properties, with errors of >> 5% observed. Therefore, until a more detailed parametric study can be carried out, we suggest that arbitrary but conservative errors of 10% are used, particularly where fault displacement is close to or below the separation limit of the dataset.

5.1. Predicting top-dyke depths from dyke-induced fault surface expressions

Our data enable us to examine how predicted top-dyke depths, estimated using several methods, compare to measured depths. For example, we test the predictive power of the trigonometry method using an average of the measured faults dips (trigα_{av}), which varies on each transect, compared to where fault dip is assumed constant (at 60° or 45°). We show that predictions of top-dyke depths made using graben width, fault dip, and/or displacement measurements are typically within error of measured top-dyke depths (Figs 6-9). Despite these similarities, predictions made using the trigα_{av} and area of loss methods typically underestimate top-dyke depths and display only a weak, positive relationship to measured top-dyke depths (R^2 = 0.26 and 0.29, respectively) (Fig. 9D). These discrepancies and weak correlation between trigα_{av} and area of loss method predictions and measured top-dyke depths relate to the incorporation of measured, as opposed to assumed, fault dip data. Fault dip measurements are susceptible to interpretation bias and vary across the fault plane over short (100–200 m) length-scales (Fig. 11A). Instead, projection of a fault with such variations in dip may be best achieved by using a constant dip representative of the entire fault. Although assuming dyke-induced faults dip consistently at 60° leads to overestimates of top-dyke depths, our data do show that assuming a consistent dip of 45° provides a good fit between predicted and measured top-dyke depths, likely because it is similar to the mean (41°) of all fault dip measurements (Figs 9D and 11B). Our data support previous studies that use constant fault dips to predict top-dyke depths (e.g., Hjartardóttir et al., 2016), implying we can relate the surface expression of dyke-induced faults, at least to some extent, to underlying dyke geometry (cf. Magee & Jackson, 2020b). However, we note that without 3D imaging of dyke-induced fault planes, we cannot ascertain whether the average of fault dips measured at a single surface (e.g., a planetary surface), or an assumed fault dip (e.g., 60° or 45°), are representative of its dip variations with depth. For example, if fault dips continuously decrease with depth, such that the faults are concave-upwards, assuming fault dip is constant will result in overestimating top-dyke depths (Magee & Jackson, 2020b).

5.1.1. Top-dyke depths

Dyke upper tips are currently located ~3.3–3.8 km below sea-level (Figs 6-9), and extended upwards to depths of at least ~1 km when they were intruded, assuming horizon HK marks the syn-emplacement free surface (Magee & Jackson, 2020a, Magee & Jackson, 2020b). Both our measurements and predictions suggest top-dyke depths vary along-strike by several hundred metres, with changes either being abrupt or gradual over several kilometres (Figs 6-9). Abrupt changes in along-strike top-dyke depths are within error, and so they could be an artefact of our interpretation (Figs 6-9). However, dykes B and E, and to a lesser extent Dyke D, show systematic increases and decreases in upper tip depth of up to ~300 m, with wavelengths of several kilometres (Figs 6-9); similar fluctuations in top-dyke tip depth, albeit on length scales of 10's of kilometres, have been shown for other members of the Exmouth Dyke Swarm (Magee & Jackson, 2020a) and for dykes in Elysium Fossae, Mars (Rivas-Dorado et al., 2021). Kilometre-scale, along-strike variations in top-dyke depth have been observed in recent dyking episodes (e.g., Ágústsdóttir et al., 2016, Trippanera et al., 2019, Xu et al., 2016), and may be a common feature of dyke swarms (e.g., Magee & Jackson, 2020a, Rivas-Dorado et al., 2021).

There are several reasons why the upper tip depth of laterally propagating dykes may increase and decrease along-strike. For example, a head region may develop at the propagating edge of a dyke, which is taller and reaches a shallower level than the tail (Figs 12A and B) (e.g., Rivalta et al., 2015, Rivas-Dorado et al., 2021). If the seismic expression of the intrusions corresponds to multiple, adjacent dykes (Magee & Jackson, 2020a), differences in the distance each dyke propagated could cause top-dyke depths to vary beneath the graben (Fig. 12A) (Rivas-Dorado et al., 2021). Alternatively, propagation of a dyke (with or without a head) may have stalled, leading to its crystallisation and pressurisation until magma broke out from dyke 'nose' to form a new segment that grew laterally and vertically (Fig. 12B) (Healy et al., 2018, Magee & Jackson, 2020b). A transition to vertical or inclined magma flow towards dyke tops can also cause dyke upper tips to segment and locally propagate vertically, affecting dyke height (e.g., Poland et al., 2008). Such dyke segmentation can particularly occur when emplacement occurs beneath a volcano load (Fig. 12C) (e.g., Poland et al., 2008), as the sloping topography results in changes to the lithostatic stresses above and along underlying dykes (Urbani et al., 2017). Density layering in the host rock is another relevant factor that controls the vertical stability of dykes, and therefore their depths; stratified host rocks are more likely to contain dykes with smaller vertical extents, which are stable under a wider range of conditions (Pollard & Townsend, 2018). Lateral changes in the vertical stratigraphic sequence may thus control how close to the free surface a dyke may reach. Finally, increases or decreases in magma density may cause dyke upper tips to become unstable and adjust to a new structural levels (Fig. 12D) (e.g., Townsend et al., 2017). Regardless of the driving mechanism, areas where top-dyke depths become shallower may focus magma flow and promote local upwards propagation, potentially leading to and explaining the restricted distribution of fissure eruptions along dyke lengths (e.g., Pansino et al., 2019, Woods et al., 2019).

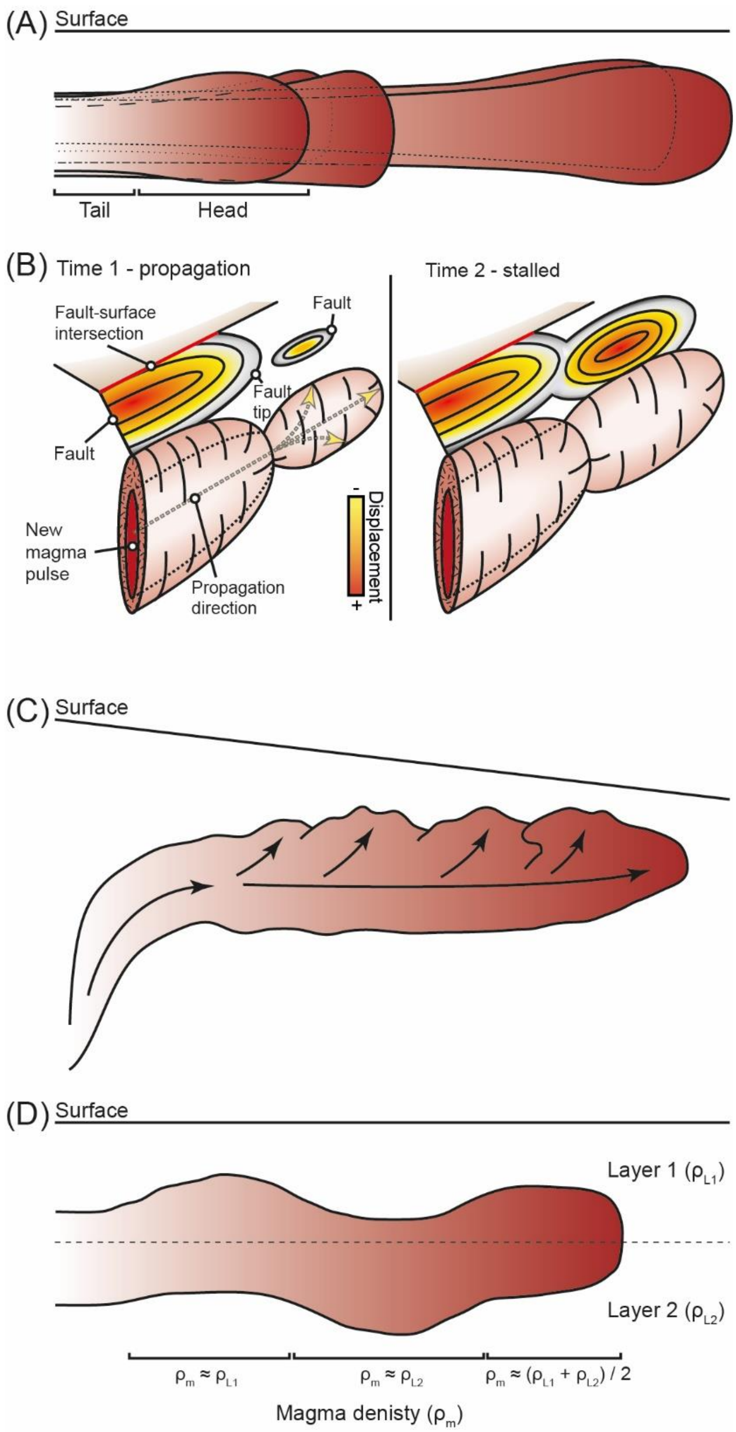

Figure 12: Possible mechanisms for changing top-dyke depths along-strike. (A) Laterally propagating dykes develop a head region that is taller and extends to shallower levels than the tail behind (modified from Rivas-Dorado et al., 2021). (B) Cyclical stalling and propagation of the dyke leads to magma breaking out from the dyke 'nose', where it is vertically restricted (Magee & Jackson, 2020b). (C) Under a variable volcano load, the ascent and lateral propagation of a dyke results in segmentation of its upper tip, which locally focuses magma flow and drives upward propagation (modified from Poland et al., 2008). (D) Changes in magma density, relative to that of a host rock displaying a density stratification,

can cause the upper and lower tip positions of a propagating dyke to destabilize and transgress upwards or downwards (Townsend et al., 2017). Where the magma density is equal to the average of two host rock layers of different densities, the dyke upper and lower tips are equally spaced from the layer boundary (Townsend et al., 2017). If magma density changes (e.g., through vesiculation, crystallisation, and/or cooling) and becomes closer in density to one of the layer, it will preferentially intrude within that layer, causing the upper and lower tips to move (Townsend et al., 2017).

5.2. Dyke-induced fault growth and kinematics

Field- and geophysical-based observations, coupled with physical, analytical, and numerical models suggest dyke-induced faults probably nucleate either: (1) near the surface, initiating as vertical tensile fractures that propagate downwards and develop into shear fractures (Fig. 13A) (e.g., Al Shehri & Gudmundsson, 2018, Trippanera et al., 2015a, Trippanera et al., 2015b, Von Hagke et al., 2019); (2) as shear fractures that grow upwards from dyke upper tips (Fig. 13B) (e.g., Koehn et al., 2019, Rubin, 1992, Xu et al., 2016); (3) at both the surface and dyke upper tip, linking as they propagate downwards and upwards, respectively (Fig. 13C) (Rowland et al., 2007, Tentler, 2005); or (4) between the surface and dyke tip, propagating both upwards and downwards (Fig. 13D) (Koehn et al., 2019, Magee & Jackson, 2020b, Mastin & Pollard, 1988).

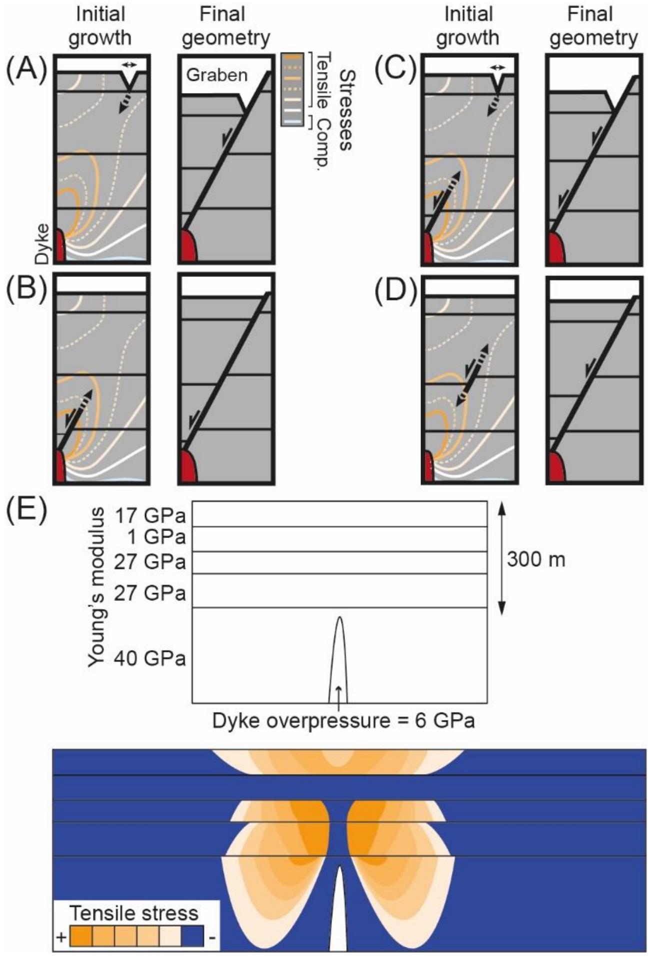

Figure 13: (A-D) Dyke-induced fault growth models (based on Koehn et al., 2019, Magee & Jackson, 2020b, Mastin & Pollard, 1988, Rubin & Pollard, 1988, Tentler, 2005, Trippanera et al., 2015b). Horizontal stress patterns above an intruding dyke in a homogeneous elastic medium, showing tensile stress is concentrated at the surface and above the dyke tip (redrawn from Rubin & Pollard, 1988). (E) Numerical model of tensile stresses above a dyke arrested at 300 m below the surface, with an overpressure of 6 GPa, in a layered medium (redrawn from Al Shehri & Gudmundsson, 2018; their Fig. 21). Tensile stresses are concentrated above the dyke tip and in two zones at the surface, but the presence of layering disrupts its distribution; e.g., the weak layer, which has a Young's modulus of 1 GPa, suppresses stress concentration (Al Shehri & Gudmundsson, 2018).

If we expect displacement to be greatest where faults nucleate (e.g., Pollard & Segall, 1987, Trippanera et al., 2015b), our mapped displacement distributions suggest fault segments initially developed between the dyke upper tip and coeval free surface (Figs 10A and C) (Koehn et al., 2019, Magee

& Jackson, 2020b, Mastin & Pollard, 1988). Yet dyke opening induces tensile stresses in the overburden, focused at the dykes upper tip and in two zones at the free surface, where modelling suggest fault nucleation most likely to occur (Fig. 1A) (e.g., Koehn et al., 2019, Pollard et al., 1983, Rubin, 1992, Rubin & Pollard, 1988). However, these models assume dyke intrusion occurs within a homogenous, elastic half-space (e.g., Koehn et al., 2019, Pollard et al., 1983, Rubin, 1992, Rubin & Pollard, 1988). Where mechanical layers with different physical properties are modelled above dykes, tensile stresses have been shown to become concentrated in relatively strong units away from the dyke tip or free surface (Fig. 13E) (Al Shehri & Gudmundsson, 2018). The dyke-induced faults we analyse primarily offset heterolithic fluvio-deltaic rocks (e.g., Bilal et al., 2018, Martin et al., 2018), as well as Jurassic sandstones and claystones (Figs 2B, 3A and B) (Tindale et al., 1998). The layered sedimentary succession offset by the dyke-induced faults is thus likely mechanically heterogeneous, which could have affected stress distribution and fault nucleation during dyking (e.g., Al Shehri & Gudmundsson, 2018, Schöpfer et al., 2006). Alternatively, displacement may preferentially accrue on faults away from their nucleation site if post-emplacement dyke thickening instigated slip (Magee & Jackson, 2020b); in this scenario, displacement distribution cannot be used to reconstruct dyke-induced fault kinematics. Overall, we suggest it likely there are multiple controls on where dyke-induced faults nucleate, which could make it difficult to assess their relation to dyke emplacement and structure.

6. Conclusions

Dyke-induced faults are common in many volcanic settings on Earth and other planetary bodies (e.g., Mars). Because we often have no or little access to the subsurface in these locations, relating the surface expression of dyke-induced faults to the underlying dyke geometry can provide key insight into the 3D structure of and processes active during dyke emplacement. However, deriving dyke geometry from the surface expression of dyke-induced faults is only feasible if the faults project straight down-dip to the dyke upper tip. Yet recent analysis of 3D seismic reflection imagery suggests dyke-induced faults are non-planar. We show that interpretation bias does introduce uncertainty into the quantitative analysis of dyke-induced faults using seismic reflection data, but that we can still use these data to confidently understand dyke and dyke-induced fault structure in 3D. By quantitatively measuring dyke-induced fault and graben geometries, we demonstrate that: (1) predictions of top-dyke depths are typically within error of measured top-dyke depths, but most accurate when incorporating information on the average dip of entire faults; and (2) dyke-induced fault displacement and dip are variable along-strike and down-dip. Our work supports previous findings and relates dyke-induced faulting to the nucleation of isolated segments above propagating dyke segments, which linked as they grew in response to dyke stalling and thickening. Cyclical dyke propagation and stalling, or other processes leading to the emplacement of dyke segments, may also explain the hectometre-scale variation in dyke upper tip depths we observe along dyke strike. Overall, our work suggests that we can relate the surface expression of dyke-induced faults to subsurface dyke geometry, but only if we have some information on the 3D structure of the faults. Reflection seismology is a critical tool for developing our understanding of dyke-induced faulting.

Acknowledgements

CM is grateful to funding from a NERC Independent Research Fellowship (NE\R014086\1) and to Geoscience Australia for making all seismic reflection and borehole datasets publically available. We also acknowledge Schlumberger for provision of the seismic interpretation software Petrel and Dug Insight for the provision of the seismic interpretation software.

Author contributions

CM conceived and designed the work, acquired the data, contributed to data analysis and interpretation, and wrote the manuscript. Both VL and KF were involved in project design and data analysis, and proof-read the manuscript. BA, SR-D, CO, and EB were involved in data analysis and interpretation, and critically revised the manuscript.

Data availability statement

Seismic reflection and borehole data used in this study are freely available from either the Geoscience Australia NOPIMS (https://nopims.dmp.wa.gov.au/nopims) data repository or that of the UK

National Geoscience Data Centre (NGDC; https://www.bgs.ac.uk/geological-data/national-geoscience-data-centre/). The NOPIMS data access centre allows “Wells” (i.e., for this study Chandon-1, Chandon-2, Chandon-3, Yellowglen 1, Briseis-1, Dunlop-1, Elfin-1, Glencoe-1, and Toporoa-1) and “Surveys” (i.e., for this study the Chandon 3D MSS and Glencoe 3D seismic reflection surveys) from offshore Australia to be searched for. From these search results, borehole data can be downloaded by highlighting the correct borehole and using “view details for selected rows”; due to the file size of 3D seismic reflection segy data, few can be downloaded but all can be added to a basket and requested from Geoscience Australia. These data can also be downloaded from the NGDC under the title “3D seismic reflection surveys (Chandon and Glencoe) and borehole data from offshore NW Australia.” All measurements and calculations acquired during this research, as well as mapped seismic horizons, are provided as supplementary information or hosted by the NGDC (Magee, 2022, Magee & Love, 2021).

References

Ágústsdóttir, T., Woods, J., Greenfield, T., Green, R. G., White, R. S., Winder, T., . . . Soosalu, H. (2016). Strike-slip faulting during the 2014 Bárðarbunga-Holuhraun dike intrusion, central Iceland. *Geophysical Research Letters*, *43*(4), 1495-1503.

Al Shehri, A., & Gudmundsson, A. (2018). Modelling of surface stresses and fracturing during dyke emplacement: Application to the 2009 episode at Harrat Lunayyir, Saudi Arabia. *Journal of Volcanology and Geothermal Research*, *356*, 278-303.

Alcalde, J., & Bond, C. E. (2022). Subjective uncertainty and biases: The impact on seismic data interpretation. In *Interpreting Subsurface Seismic Data* (pp. 103-123). Elsevier.

Alcalde, J., Bond, C. E., Johnson, G., Ellis, J. F., & Butler, R. W. (2017). Impact of seismic image quality on fault interpretation uncertainty. *GSA Today*.

Alcalde, J., Bond, C. E., Johnson, G., Kloppenburg, A., Ferrer, O., Bell, R., & Ayarza, P. (2019). Fault interpretation in seismic reflection data: an experiment analysing the impact of conceptual model anchoring and vertical exaggeration. *Solid Earth*, *10*(5), 1651-1662.

Alcalde, J., Bond, C. E., & Randle, C. H. (2017). Framing bias: The effect of figure presentation on seismic interpretation. *Interpretation*, *5*(4), T591-T605.

Allen, P. A., & Allen, J. R. (2013). *Basin analysis: Principles and application to petroleum play assessment*. John Wiley & Sons.

Anderson, E. M. (1951). *The dynamics of faulting and dyke formation with applications to Britain*. Hafner Pub. Co.

Andrews, B. J., Roberts, J. J., Shipton, Z. K., Bigi, S., Tartarello, M. C., & Johnson, G. (2019). How do we see fractures? Quantifying subjective bias in fracture data collection. *Solid Earth*, *10*(2), 487-516.

Bilal, A., & McClay, K. (2022). Tectonic and stratigraphic evolution of the central Exmouth Plateau, NW Shelf of Australia. *Marine and Petroleum Geology*, *136*, 105447.

Bilal, A., McClay, K., & Scarselli, N. (2018). Fault-scarp degradation in the central Exmouth Plateau, North West Shelf, Australia. *Geological Society, London, Special Publications*, *476*, SP476. 411.

Black, M., McCormack, K., Elders, C., & Robertson, D. (2017). Extensional fault evolution within the Exmouth Sub-basin, North West Shelf, Australia. *Marine and Petroleum Geology*, *85*, 301-315.

Bond, C. E., Gibbs, A. D., Shipton, Z. K., & Jones, S. (2007). What do you think this is?``Conceptual uncertainty"in geoscience interpretation. *GSA today*, *17*(11), 4-10.

Bond, C. E., Johnson, G., & Ellis, J. (2015). Structural model creation: the impact of data type and creative space on geological reasoning and interpretation. *Geological Society, London, Special Publications*, *421*(1), 83-97.

Bosworth, W., Stockli, D. F., & Helgeson, D. E. (2015). Integrated outcrop, 3D seismic, and geochronologic interpretation of Red Sea dike-related deformation in the Western Desert, Egypt–The role of the 23Ma Cairo “mini-plume”. *Journal of African Earth Sciences*, *109*, 107-119.

Brown, A. R. (2011). *Interpretation of three-dimensional seismic data* (6th ed., Vol. 42). AAPG and SEG.

Delogkos, E., Manzocchi, T., Childs, C., Sachanidis, C., Barbas, T., Schöpfer, M. P., . . . Walsh, J. J. (2017). Throw partitioning across normal fault zones in the Ptolemais Basin, Greece. *Geological Society, London, Special Publications*, *439*(1), 333-353.

Dimmen, V., Rotevatn, A., & Lecomte, I. (2022). Imaging of small-scale faults in seismic reflection data: Insights from seismic modelling of faults in outcrop. *Marine and Petroleum Geology*, 105980.

Direen, N. G., Stagg, H. M. J., Symonds, P. A., & Colwell, J. B. (2008). Architecture of volcanic rifted margins: new insights from the Exmouth – Gascoyne margin, Western Australia. *Australian Journal of Earth Sciences*, *55*(3), 341-363. https://doi.org/10.1080/08120090701769472

Dumont, S., Klinger, Y., Socquet, A., Doubre, C., & Jacques, E. (2017). Magma influence on propagation of normal faults: Evidence from cumulative slip profiles along Dabbahu-Manda-Hararo rift segment (Afar, Ethiopia). *Journal of Structural Geology*, *95*, 48-59.

Dumont, S., Socquet, A., Grandin, R., Doubre, C., & Klinger, Y. (2016). Surface displacements on faults triggered by slow magma transfers between dyke injections in the 2005–2010 rifting episode at Dabbahu–Manda–Hararo rift (Afar, Ethiopia). *Geophysical Journal International*, *204*(1), 399-417.

Exon, N., Haq, B., & Von Rad, U. (1992). Exmouth Plateau revisited: scientific drilling and geological framework. Proceedings of the Ocean Drilling Program, Scientific Results,

Faleide, T. S., Braathen, A., Lecomte, I., Mulrooney, M. J., Midtkandal, I., Bugge, A. J., & Planke, S. (2021). Impacts of seismic resolution on fault interpretation: Insights from seismic modelling. *Tectonophysics*, *816*, 229008.

Gartrell, A., Torres, J., Dixon, M., & Keep, M. (2016). Mesozoic rift onset and its impact on the sequence stratigraphic architecture of the Northern Carnarvon Basin. *The APPEA Journal*, *56*(1), 143-158.

Gibson, H., Stewart, I. S., Pahl, S., & Stokes, A. (2016). A" mental models" approach to the communication of subsurface hydrology and hazards. *Hydrology and Earth System Sciences*, *20*(5), 1737-1749.

Hardy, S. (2016). Does shallow dike intrusion and widening remain a possible mechanism for graben formation on Mars? *Geology*, *44*(2), 107-110.

Healy, D., Rizzo, R., Duffy, M., Farrell, N. J., Hole, M. J., & Muirhead, D. (2018). Field evidence for the lateral emplacement of igneous dykes: Implications for 3D mechanical models and the plumbing beneath fissure eruptions. *Volcanica*, *1*(2), 85-105. https://doi.org/10.30909/vol.01.02.85105

Hjartardóttir, Á. R., Einarsson, P., Gudmundsson, M. T., & Högnadóttir, T. (2016). Fracture movements and graben subsidence during the 2014 Bárðarbunga dike intrusion in Iceland. *Journal of Volcanology and Geothermal Research*, *310*, 242-252.

Hocking, R. M., Moors, H. T., & Van de Graaff, W. E. (1987). *Geology of the carnarvon basin, Western Australia* (Vol. 133). State Print. Division.

Karner, G. D., & Driscoll, N. W. (1999). Style, timing and distribution of tectonic deformation across the Exmouth Plateau, northwest Australia, determined from stratal architecture and quantitative basin modelling. In C. MacNiocall & P. Ryan (Eds.), *Continental Tectonics. Geological Society, London, Special Publications* (Vol. 164, pp. 271-311). Geological Society of London.

Koehn, D., Steiner, A., & Aanyu, K. (2019). Modelling of extension and dyking-induced collapse faults and fissures in rifts. *Journal of Structural Geology*, *118*, 21-31.

Longley, I., Buessenschuett, C., Clydsdale, L., Cubitt, C., Davis, R., Johnson, M., . . . Spry, T. (2002). The North West Shelf of Australia–a Woodside perspective. *The sedimentary basins of Western Australia*, *3*, 27-88.

Macrae, E. J., Bond, C. E., Shipton, Z. K., & Lunn, R. J. (2016). Increasing the quality of seismic interpretation. *Interpretation*, *4*(3), T395-T402.

Magee, C. (2022). *Dyke-induced fault and pit crater measurements and predicted dyke properties offshore NW Australia*. https://doi.org/10.5285/2edf6c47-fd18-4540-b449-b78d12422193

Magee, C., Duffy, O. B., Purnell, K., Bell, R. E., Jackson, C. A. L., & Reeve, M. T. (2016). Fault-controlled fluid flow inferred from hydrothermal vents imaged in 3D seismic reflection data, offshore NW Australia. *Basin Research*, *28*(3), 299-318.

Magee, C., & Jackson, C.-L. (2020). Seismic reflection data reveal the 3D structure of the newly discovered Exmouth Dyke Swarm, offshore NW Australia. *Solid Earth*, *11*(2), 576-606.

Magee, C., & Jackson, C. A.-L. (2020). Can we relate the surface expression of dike-induced normal faults to subsurface dike geometry? *Geology*, *49*. https://doi.org/10.1130/G48171.1

Magee, C., Kling, C. L., Byrne, P. K., & Jackson, C. (2022). Seismic reflection data reveal the 3D subsurface structure of pit craters. *Journal of Geophysical Research: Planets*, *127*, e2021JE007155.

Magee, C., & Love, V. (2021). *Dyke-induced fault measurements and predicted dyke properties offshore NW Australia*. https://doi.org/10.5285/f8c2c92a-450d-49e7-bfac-9317d2828e33

Mansfield, C. S., & Cartwright, J. A. (1996). High resolution fault displacement mapping from three-dimensional seismic data: evidence for dip linkage during fault growth. *Journal of Structural Geology*, *18*, 14.

Martin, J., Fernandes, A. M., Pickering, J., Howes, N., Mann, S., & McNeil, K. (2018). The stratigraphically preserved signature of persistent backwater dynamics in a large paleodelta system: The Mungaroo Formation, North West Shelf, Australia. *Journal of Sedimentary Research*, *88*(7), 850-872.

Mastin, L. G., & Pollard, D. D. (1988). Surface deformation and shallow dike intrusion processes at Inyo Craters, Long Valley, California. *Journal of Geophysical Research: Solid Earth*, *93*(B11), 13221-13235.

Norcliffe, J., Magee, C., Jackson, C., Kopping, J., & Lathrop, B. (2021). Fault inversion contributes to ground deformation above inflating igneous sills. *Volcanica*, *4*(1), 1-21.

Pansino, S., Emadzadeh, A., & Taisne, B. (2019). Dike channelization and solidification: time scale controls on the geometry and placement of magma migration pathways. *Journal of Geophysical Research: Solid Earth*, *124*(9), 9580-9599.

Paumard, V., Bourget, J., Payenberg, T., Ainsworth, R. B., George, A. D., Lang, S., . . . Peyrot, D. (2018). Controls on shelf-margin architecture and sediment partitioning during a syn-rift to post-rift transition: Insights from the Barrow Group (Northern Carnarvon Basin, North West Shelf, Australia). *Earth-Science Reviews*, *177*, 643-677.

Perrin, C., Jacob, A., Lucas, A., Myhill, R., Hauber, E., Batov, A., . . . Stevanović, J. (2022). Geometry and segmentation of Cerberus Fossae, Mars: Implications for marsquake properties. *Journal of Geophysical Research: Planets*, *127*(1), e2021JE007118.

Poland, M. P., Moats, W. P., & Fink, J. H. (2008). A model for radial dike emplacement in composite cones based on observations from Summer Coon volcano, Colorado, USA. *Bulletin of Volcanology*, *70*(7), 861-875.

Pollard, D. D., Delaney, P. T., Duffield, W. A., Endo, E. T., & Okamura, A. T. (1983). Surface deformation in volcanic rift zones. *Tectonophysics*, *94*(1-4), 541-584.

Pollard, D. D., & Segall, P. (1987). Theoretical displacements and stresses near fractures in rock: with applications to faults, joints, veins, dikes, and solution surfaces. In B. Atkinson (Ed.), *Fracture mechanics of rock* (pp. 277-347). Academic Press.

Pollard, D. D., & Townsend, M. R. (2018). Fluid-filled fractures in Earth's lithosphere: gravitational loading, interpenetration, and stable height of dikes and veins. *Journal of Structural Geology*, *109*, 38-54.

Pryer, L., Romine, K., Loutit, T., & Barnes, R. (2002). Carnarvon basin architecture and structure defined by the integration of mineral and petroleum exploration tools and techniques. *The APPEA Journal*, *42*(1), 287-309.

Rankey, E., & Mitchell, J. (2003). That's why it's called interpretation: Impact of horizon uncertainty on seismic attribute analysis. *The Leading Edge*, *22*(9), 820-828.

Reeve, M. T., Jackson, C. A. L., Bell, R. E., Magee, C., & Bastow, I. D. (2016). The stratigraphic record of prebreakup geodynamics: Evidence from the Barrow Delta, offshore Northwest Australia. *Tectonics*, *35*(8), 1935-1968.

Reeve, M. T., Magee, C., Bastow, I. D., McDermott, C., Jackson, C. A.-L., Bell, R. E., & Prytulak, J. (2021). Nature of the Cuvier Abyssal Plain crust, offshore NW Australia. *Journal of the Geological Society*.

Rivalta, E., Taisne, B., Bunger, A., & Katz, R. (2015). A review of mechanical models of dike propagation: Schools of thought, results and future directions. *Tectonophysics*, *638*, 1-42.

Rivas-Dorado, S., Ruiz, J., & Romeo, I. (2021). Subsurface Geometry and Emplacement Conditions of a Giant Dike System in Elysium Fossae, Mars. *Journal of Geophysical Research: Planets*, *126*(1), e2020JE006512.

Robb, M. S., Taylor, B., & Goodliffe, A. M. (2005). Re-examination of the magnetic lineations of the Gascoyne and Cuvier Abyssal Plains, off NW Australia. *Geophysical Journal International*, *163*(1), 42-55.

Rowland, J., Baker, E., Ebinger, C., Keir, D., Kidane, T., Biggs, J., . . . Wright, T. (2007). Fault growth at a nascent slow-spreading ridge: 2005 Dabbahu rifting episode, Afar. *Geophysical Journal International*, *171*(3), 1226-1246.

Rubin, A. M. (1992). Dike-induced faulting and graben subsidence in volcanic rift zones. *Journal of Geophysical Research: Solid Earth*, *97*(B2), 1839-1858.

Rubin, A. M. (1993). Tensile fracture of rock at high confining pressure: implications for dike propagation. *Journal of Geophysical Research: Solid Earth*, *98*(B9), 15919-15935.

Rubin, A. M., & Pollard, D. D. (1988). Dike-induced faulting in rift zones of Iceland and Afar. *Geology*, *16*(5), 413-417.

Schaaf, A., & Bond, C. E. (2019). Quantification of uncertainty in 3-D seismic interpretation: implications for deterministic and stochastic geomodeling and machine learning. *Solid earth*, *10*(4), 1049-1061.

Schöpfer, M. P. J., Childs, C., & Walsh, J. J. (2006). Localisation of normal faults in multilayer sequences. *Journal of Structural Geology*, *28*(5), 816-833. https://doi.org/http://dx.doi.org/10.1016/j.jsg.2006.02.003

Shipley, T. F., & Tikoff, B. (2016). Linking cognitive science and disciplinary geoscience practice: The importance of the conceptual model. In *3-D Structural Interpretation: Earth, Mind and Medicine* (Vol. Memoir 111). AAPG Special Volumes.

Shipton, Z. K., Roberts, J. J., Comrie, E., Kremer, Y., Lunn, R., & Caine, J. (2020). Fault fictions: Systematic biases in the conceptualization of fault-zone architecture. *Geological Society, London, Special Publications*, *496*(1), 125-143.

Stagg, H., Alcock, M., Bernardel, G., Moore, A., Symonds, P., & Exon, N. (2004). *Geological framework of the outer Exmouth Plateau and adjacent ocean basins*. Geoscience Australia.

Taylor, S. K., Nicol, A., & Walsh, J. J. (2008). Displacement loss on growth faults due to sediment compaction. *Journal of Structural Geology*, *30*(3), 394-405.

Tentler, T. (2005). Propagation of brittle failure triggered by magma in Iceland. *Tectonophysics*, *406*(1), 17-38.

Tindale, K., Newell, N., Keall, J., & Smith, N. (1998). Structural evolution and charge history of the Exmouth Sub-basin, northern Carnarvon Basin, Western Australia. The Sedimentary Basins of Western Australia 2: Proc. of Petroleum Society Australia Symposium, Perth, WA,

Townsend, M. R., Pollard, D. D., & Smith, R. P. (2017). Mechanical models for dikes: a third school of thought. *Tectonophysics*, *703*, 98-118.

Trippanera, D., Acocella, V., Ruch, J., & Abebe, B. (2015). Fault and graben growth along active magmatic divergent plate boundaries in Iceland and Ethiopia. *Tectonics*, *34*(11), 2318-2348.

Trippanera, D., Ruch, J., Acocella, V., & Rivalta, E. (2015). Experiments of dike-induced deformation: Insights on the long-term evolution of divergent plate boundaries. *Journal of Geophysical Research: Solid Earth*, *120*(10), 6913-6942.

Trippanera, D., Ruch, J., Passone, L., & Jónsson, S. (2019). Structural mapping of dike-induced faulting in Harrat Lunayyir (Saudi Arabia) by using high resolution drone imagery. *Frontiers in Earth Science*, *7*, 168.

Urbani, S., Acocella, V., Rivalta, E., & Corbi, F. (2017). Propagation and arrest of dikes under topography: Models applied to the 2014 Bardarbunga (Iceland) rifting event. *Geophysical Research Letters*, *44*(13), 6692-6701.

Von Hagke, C., Kettermann, M., Bitsch, N., Bücken, D., Weismüller, C., & Urai, J. L. (2019). The effect of obliquity of slip in normal faults on distribution of open fractures. *Frontiers in Earth Science*, *7*(18).

Wilson, C. G., Bond, C. E., & Shipley, T. F. (2019). How can geologic decision-making under uncertainty be improved? *Solid earth*, *10*(5), 1469-1488.

Wilson, L., & Head, J. W. (2002). Tharsis-radial graben systems as the surface manifestation of plume-related dike intrusion complexes: Models and implications. *Journal of Geophysical Research: Planets*, *107*(E8).

Woods, J., Winder, T., White, R. S., & Brandsdóttir, B. (2019). Evolution of a lateral dike intrusion revealed by relatively-relocated dike-induced earthquakes: The 2014–15 Bárðarbunga–Holuhraun rifting event, Iceland. *Earth and Planetary Science Letters*, *506*, 53-63.

Wright, T. J., Ebinger, C., Biggs, J., Ayele, A., Yirgu, G., Keir, D., & Stork, A. (2006). Magma-maintained rift segmentation at continental rupture in the 2005 Afar dyking episode. *Nature*, *442*(7100), 291-294. https://doi.org/10.1038/nature04978

Xu, W., Jónsson, S., Corbi, F., & Rivalta, E. (2016). Graben formation and dike arrest during the 2009 Harrat Lunayyir dike intrusion in Saudi Arabia: Insights from InSAR, stress calculations and analog experiments. *Journal of Geophysical Research: Solid Earth*, *121*(4), 2837-2851.

Yang, X.-M., & Elders, C. (2016). The Mesozoic structural evolution of the Gorgon Platform, North Carnarvon Basin, Australia. *Australian Journal of Earth Sciences*, *63*(6), 755-770.